Crustal structure of southeast Australia from teleseismic receiver functions

Mohammed Bello[1,2], David G. Cornwell[1], Nicholas Rawlinson[3], Anya M. Reading[4], Othaniel K. Likkason[2]

[1]Department Geology & Geophysics, University of Aberdeen, Aberdeen, UK
[2]Department of Physics, Abubakar Tafawa Balewa University, Bauchi, Nigeria
[3]Department of Earth Sciences, University of Cambridge, UK
[4]School of Natural Sciences (Physics), University of Tasmania, Australia

Correspondence to: Nicholas Rawlinson (nr441@cam.ac.uk)

Abstract. In an effort to improve our understanding of the seismic character of the crust beneath southeast Australia, and how it relates to the tectonic evolution of the region, we analyse teleseismic earthquakes recorded by 24 temporary and 8 permanent broadband stations using the receiver function method. Due to the proximity of the temporary stations to Bass Strait, only 13 of these stations yielded usable receiver functions, whereas seven permanent stations produced receiver functions for subsequent analysis. Crustal thickness, bulk seismic velocity properties and internal crustal structure of the southern Tasmanides – an assemblage of Palaeozoic accretionary orogens that occupy eastern Australia – are constrained by H-κ stacking and receiver function inversion, which point to: (1) a ~39.0 km thick crust, an intermediate-high Vp/Vs ratio (~1.70-1.76), relative to ak135, and a broad (>10 km) crust-mantle transition beneath the Lachlan Fold Belt. These results are interpreted to represent magmatic underplating of mafic materials at the base of the crust; (2) a complex crustal structure beneath VanDieland, a putative Precambrian continental fragment embedded in the southernmost Tasmanides, which features strong variability in crustal thickness (23-37 km) and Vp/Vs ratio (1.65-193), the latter of which likely represents compositional variability and the presence of melt. The complex origins of VanDieland, which comprises multiple continental ribbons, coupled with recent failed rifting and intraplate volcanism, likely contributes to these observations; and (3) stations located in the East Tasmania Terrane and Eastern Bass Strait (ETT+EB) collectively indicate crust of uniform thickness (31-32 km), which clearly distinguish it from VanDieland to the west. Moho depths are also compared with the continent-wide AusMoho model in southeast Australia, and are shown to be largely consistent, except in regions where AusMoho has few constraints (e.g. Flinders Island). A joint interpretation of the new results with ambient noise, teleseismic tomography and teleseismic shear wave splitting anisotropy, helps provide new insight into the way that the crust has been shaped by recent events, including failed rifting during the break-up of Australia and Antarctica and recent intraplate volcanism.

Keywords: receiver functions, crustal structure, VanDieland, Bass Strait, SE Australia

1 Introduction

The Phanerozoic Tasmanides (Collins and Vernon, 1994; Coney, 1995; Coney et al., 1990) comprise the eastern one-third of the Australian continent and through a process of subduction accretion were juxtaposed against the eastern flank of the Precambrian shield region of Australia beginning in the Late Neoproterozoic and Early Palaeozoic (Foster and Gray, 2000; Glen, 2005; Glen et al., 2009; Moresi et al., 2014) (Figure 1). Persistent

38 sources of debate that impede a more complete understanding of the geology of the Tasmanides include: (1) the
39 geological link between Tasmania – an island state in southeast Australia – and mainland Australia, which are
40 separated by the waters of Bass Strait; and (2) the presence and locations of continental fragments from
41 Rodinian remnants that are entrained within the accretionary orogens. Furthermore, the lateral boundaries
42 between individual tectonic blocks and their crustal structure are often not well defined. To date, few constraints
43 on crustal thickness and seismic velocity structure have been available for regions such as Bass Strait.
44 Constraints on the Moho transition, crustal thickness and velocity structure beneath Bass Strait derived from
45 receiver functions (RFs) can therefore provide fresh insight into the nature and evolution of the Tasmanides.

46 Previous estimates of crustal thickness and structure beneath southeastern Australia have been obtained from
47 deep seismic reflection transects, wide-angle seismic data, topography and gravity anomalies (e.g. Collins,
48 1991; Collins et al., 2003; Drummond et al., 2006 and Kennett et al., 2011). Earlier RF studies in southeast
49 Australia (Shibutani et al., 1996; Clitheroe et al., 2000; Tkalčić et al., 2011; Fontaine et al., 2013a,b) suggested
50 the presence of complex lateral velocity variations in the mid-lower crust that probably reflect the interaction of
51 igneous underplating, associated thinning of the lithosphere, recent hotspot volcanism and uplift. Furthermore,
52 the intermediate to high crustal Vp/Vs ratio of 1.70–1.78 in this region (Fontaine et al., 2013a), relative to ak135
53 continental crust where Vp/Vs is $\sim$1.68, may indicate a mafic composition that includes mafic granulite rocks,
54 granite-gneiss and biotite gneiss. Body- and surface-wave tomography (Fishwick and Rawlinson, 2012;
55 Rawlinson et al., 2015) revealed P and S wave velocity anomalies in the uppermost mantle beneath Bass Strait
56 and the Lachlan Fold Belt. Ambient noise surface wave tomography (Bodin et al., 2012b; Young et al., 2012;
57 Pilia et al., 2015b, 2016; Crowder et al., 2019) of the southern Tasmanides revealed significant crustal
58 complexity, but is unable to constrain crustal thickness or the nature of the Moho transition.

59 The goal of this paper is to provide fresh insight into the crust and Moho structure beneath the southern
60 Tasmanides using P-wave RFs and explain the origin of the lateral heterogeneities that are observed. This will
61 allow us to explore the geological relationship between the different tectonic units that constitute the southern
62 Tasmanides, and develop an improved understanding of the region's tectonic history.

63 **2 Geological setting**

64 The Palaeozoic-Mesozoic Tasmanides of eastern Australia form part of one of the most extensive accretionary
65 orogens in existence and evolved from interaction between the East Gondwana margin and the Proto-Pacific
66 Ocean. The tectonic evolution of the Tasmanides is complex and large-scale reconstructions have proven
67 difficult. This is evident from the variety of models that have been suggested to explain how the region formed
68 (Foster and Gray, 2000; Spaggiari et al., 2003; Teasdale et al., 2003; Spaggiari et al., 2004; Boger and Miller,
69 2004; Glen, 2005; Cawood, 2005; Glen et al., 2009; Cayley, 2011a,b; Gibson et al., 2011; Moresi et al., 2014;
70 Pilia et al., 2015a,b). Particular challenges arise from multiple subduction events, multiple phases of
71 metamorphism, entrainment of exotic continental blocks, the formation of large oroclines, recent intraplate
72 volcanism and subsequent events, including the separation of Antarctica and Australia and the formation of the
73 Tasman Sea. These challenges are compounded by the presence of widespread sedimentary sequences that
74 hinder direct access to basement rocks (Fig. 1).

75 The Tasmanides consist of four orogenic belts, namely the Delamerian, Lachlan, Thomson and New England

76 Orogens. The Delamerian Orogen - located in the south - is the oldest part of the Tasmanides and has a

77 southward extension across Bass Strait from Victoria into western Tasmania, where it is commonly referred to

78 as the Tyennan Orogen (Berry et al., 2008). Between about 514 and 490 Ma, the Precambrian and Early

79 Cambrian rocks that constitute the Delamerian Orogen were subjected to a contractional orogenic event along

80 the margin of East Gondwana (Foden et al., 2006). Subsequently, the Lachlan Orogen formed in the east, which

81 contains rocks that vary in age from Ordovician to Carboniferous (Glen, 2005). Gray and Foster (2004) argued

82 for a tectonic model of the Lachlan Orogen that involved interaction of a volcanic arc, oceanic microplates and

83 three distinct subduction zones. Each subduction zone is linked to the formation of a distinct tectonic terrain: the

84 Stawell-Bendigo zone, Tabbarebbera zone and Narooma accretionary complex. The limited rock exposure in the

85 Tasmanides as a whole has made direct observation of the Lachlan Orogen difficult; this is attributed to a large

86 swath of Mesozoic-Cenozoic sedimentary cover and more recent Quaternary volcanics, which obscure a large

87 portion of the underlying Palaeozoic terrane. However, the Lachlan Orogen contains belts of Cambrian rocks in

88 Victoria and New South Wales that are similar in age to the Delamerian Orogen (Gray and Foster, 2004).

89 The presence of Precambrian outcrops in Tasmania and the relative lack of similar age rocks in adjacent

90 mainland Australia has led to different models which attempted to explain the existence of Proterozoic

91 Tasmania. For instance, Li et al. (1997) suggested that western Tasmania may be the remnant of a continental

92 fragment set adrift by Rodianian break-up, whereas Calvert and Walter (2000) proposed that King Island, along

93 with western Tasmania, rifted away from the Australian craton around ~600 Ma (Fig. 1). Other researchers have

94 developed scenarios in which the island of Tasmania was present as a separate microcontinental block that was

95 positioned outboard of the eastern margin of Gondwana before re-attaching at the commencement of the

96 Palaeozoic (Berry et al., 2008).

97 A popular model that attempts to reconcile the geology observed in Tasmania and adjacent mainland Australia

98 is that of Cayley (2011a). This model proposes that central Victoria and western Tasmania formed a

99 microcontinental block called "VanDieland" that fused with East Gondwana at the end of the Cambrian,

100 possibly terminating the Delamerian Orogeny. VanDieland became entangled in the subduction-accretion

101 system which built the Palaeozoic orogens that now comprise eastern Australia (Fig. 1). Delineating

102 Precambrian continental fragments within southeast Australia has proven difficult, partly due to more recent

103 sedimentary cover that obscures large tracts of the Tasmanides. However, if present, they likely have distinctive

104 structural and seismic velocity characteristics (Glen, 2013).

105 **3 Previous geophysical studies**

106 A variety of geophysical methods have so far been employed to study the crustal structure of the Tasmanides.

107 Shibutani et al. (1996) applied a non-linear inversion method to RF waveforms to constrain the shear wave

108 velocity beneath broadband seismic stations in eastern Australia. They found that the Moho is relatively shallow

109 (30-36 km depth) and sharp within the cratonic region, and deeper (38-44 km) and transitional along the axis of

110 the Tasmanides. They suggested that crustal thickening of the fold belt by underplating or intrusion of mantle

111 materials may have contributed to this observation. Clitheroe et al. (2000) built on this earlier work by inverting

112 RFs to map broad-scale crustal thickness and Moho character across the Australian continent. They found that in

general, there was good agreement between xenolith-derived estimates of Moho depth and those determined by RF inversion, except beneath the Lachlan Fold Belt, where a broad Moho transition may be present. Overall, however, the RF results were consistent with those determined by Drummond and Collins (1986) and Collins (1991), who used seismic reflection and refraction transects to determine that the Lachlan Fold Belt includes the thickest crust (~50 km) in eastern Australia. A more recent study by Fontaine et al. (2013a) employed H-κ stacking and non-linear RF inversion to investigate crustal thickness, shear wave velocity structure, as well as dipping and anisotropy of the crustal layers. Their results also indicated a thick crust (~48 km) and an intermediate (2-9 km) crust-mantle transition beneath the Lachlan Fold Belt, which could be attributed to underplating beneath the crust and/or high concentrations of mafic rocks in the mid-lower crust. Their results also showed a dipping Moho together with crustal anisotropy in the vicinity of three seismic stations (YNG, CNB and CAN).

Over the last decade, ambient noise tomography has become a popular tool for studying the structure of the Australian crust. Saygin and Kennett (2010) produced the first group velocity maps of the Australian continent from Rayleigh wave group velocity dispersion in the period range 5.0–12.5 seconds. Limited spatial resolution (~ 2º x 2º) in our study region means that this model is only able to represent the structure beneath Bass Strait as a broad, low velocity anomaly. However, the group velocities exhibit a good correlation with known basins and cratons. Subsequent studies using denser arrays covering southeast mainland Australia (Arroucau et al., 2010), southeastern Australia (Young et al. 2013), and northern Tasmania (Young et al., 2011) show good correlations between group/phase velocity maps and sedimentary and basement terrane boundaries. In order to account for uneven data distribution, Bodin et al. (2012b) used a Bayesian transdimensional inversion scheme to generate group velocity maps that span the Australian continent from multi-scale ambient noise datasets. However, in our study area their model is of low resolution due to the limited station coverage and hence few details on crustal structure can be inferred. Bodin et al. (2012a) subsequently applied Bayesian statistics to reconstruct the Moho geometry of Australia using a variety of seismic datasets, which gave an approximate Moho depth of ~30 km beneath Bass Strait. Pilia et al. (2015a,b) and Crowder et al. (2019) derived 3-D shear wave velocity models of the Bass strait region using ambient noise data from the same array of temporary stations that we exploit in this study. They were able to constrain the lateral and depth extent of the primary sedimentary basins in the region, and provide insight into the seismic character of the Precambrian micro-continental block that appears to underpin southern Victoria, north western Tasmania and Bass Strait.

Teleseismic tomography has also been used to image the lithosphere beneath southeast Australia, thanks in part to the prolific deployment of short-period seismometers as part of the WOMBAT transportable array project (Rawlinson and Kennett, 2008, Rawlinson et al., 2015, 2016). While the main focus has been on the upper mantle, in Tasmania, where station spacing was denser, some constraints on crustal velocity structure were possible. Rawlinson et al. (2006) found that the crust beneath the ETT was significantly faster than the crust beneath central Tasmania, which may represent a contrast between crust with oceanic provenance in the east and Precambrian continental provenance in the west. Bello et al. (2019b) built on this work by including teleseismic arrival time data from the same temporary deployment as the the current study to generate a detailed upper mantle model of southeast Australia, which revealed that Bass Strait was underlain by lower velocities, consistent with thinned lithosphere as a result of failed rifting during the break-up of Australia and Antarctica.

4

152 Active source seismic profiling has also been widely used in southeast Australia to characterize crustal velocity
153 structure (e.g. Finlayson et al., 1980; Collins, 1991; Finlayson et al., 2002; Drummond et al., 2006; Glen, 2013).
154 This has largely focused on the transition from continental to oceanic crust at passive margins, but has also been
155 used to image major transition zones or faults between orogens (Glen, 2013) or within orogens (Cayley et al.,
156 2011a,b), the latter of which lead to the VanDieland microcontinental model. Rawlinson and Urvoy (2006)
157 jointly inverted teleseismic arrival times and active source wide-angle traveltimes in northern Tasmania to
158 constrain crustal velocity, Moho geometry and upper mantle velocity structure and found that both northeastern
159 and northwestern Tasmania is characterised by thinner (<28 km) and higher velocity crust compared to central
160 Tasmania.

161 Potential field data have also been exploited to study the formation and structure of the Tasmanides. Gunn et al.
162 (1997) integrated potential field data (magnetic and gravity), seismic reflection data, outcrop geology and well
163 information to study the crustal structure of the Australian continent. Their study found that the occurrence of
164 tensional stress, oriented NE-SW along basement structures in the Bass Basin, is able to explain the formation of
165 the three major sedimentary basins that overlie dense mafic material, which in turn was formed by mantle
166 decompression processes associated with crustal stretching. From the interpretation of new aeromagnetic data,
167 Morse et al. (2009) delineated the architecture of the Bass Strait basins and their supporting basement structure.
168 Subsequent studies by Moore et al. (2015, 2016) used gravity, magnetic, seismic reflection and outcrop data to
169 support the hypothesis of a VanDieland microcontinent. Their study showed that VanDieland comprises seven
170 distinct microcontinental ribbon terranes that appear to have amalgamated by the Late Cambrian, with major
171 faults and suture zones bonding these ribbon terranes together.

172 While the last few decades have seen important advances and insights made into our understanding of the
173 southern Tasmanides, there still remains limited data on the deep crustal structure beneath Bass Strait, which is
174 our region of interest. It is therefore timely that we can exploit, using the RF technique, teleseismic data
175 recorded by a collection of temporary and permanent seismic stations in the region to study the structure of the
176 crust, Moho and uppermost mantle beneath mainland Australia, Bass Strait and Tasmania.

177 **4 Data**

178 A collaboration involving five organisations (University of Tasmania, Australian National University, Mineral
179 Resources Tasmania, the Geological Survey of Victoria and FROGTECH) deployed the temporary Bass seismic
180 array from May 2011 to April 2013. It consisted of 24 broadband, three-component seismic stations that
181 spanned northern Tasmania, and a selection of islands in Bass Strait and southern Victoria. The instruments
182 used were 23 Güralp 40T and one Güralp 3ESP sensors coupled to Earth Data PR6-24 data loggers. The
183 permanent stations consist of eight broadband sensors managed by IRIS, GEOSCOPE and the Australian
184 National Seismic Network (ANSN). The distribution of all 32 seismic stations that are used in this study is
185 plotted in Figure 2. Earthquakes with magnitudes $m_b > 5.5$ at epicentral distances between 30° and 90° comprise
186 the seismic sources used in this analysis (Fig. 3). This resulted in an acceptable azimuthal coverage of
187 earthquakes between the northwest and east of the array, where active convergence of the Australian and
188 Eurasian plate coupled with westward motion of the Pacific plate has produced extensive subduction zones. To
189 the south and southwest of the array, the absence of subduction zones in the required epicentral distance range

190 means that there are significantly fewer events available for analysis from these regions.

191 **5 Methods**

192 **5.1 Receiver functions**

193 The RF technique (Langston, 1979) uses earthquakes at teleseismic distances to enable estimation of Moho
194 depth and shear wave velocity structure in the vicinity of a seismic recorder. If this technique can be applied to a
195 network of stations with good spatial coverage, it represents an effective way of mapping lateral variations in
196 Moho depth and crustal structure.

197 A recorded teleseismic wavefield at a broadband station can be described by the convolutional model in which
198 operators that represent the source radiation pattern, path effects, crustal structure below the station and
199 instrument response are combined to describe the recorded waveform. By using deconvolution to remove the
200 effects of the source, path and response of the instrument (e.g. Langston, 1979), information on local crustal
201 structure beneath the station can be extracted from *P-S* wave conversions at discontinuities in seismic velocity
202 (Owens et al., 1987; Ammon, 1991).

203 *P*-wave RFs were determined from teleseismic *P*-waveforms using FuncLab software (Eagar and Fouch, 2012;
204 Porritt and Miller, 2018), following preprocessing using the seismic analysis code (SAC) (Goldstein et al.,
205 2003). RFs were computed by applying an iterative time-domain deconvolution scheme developed by Ligorria
206 and Ammon (1999) with a 2.5 s Gaussian filter width. This is achieved by deconvolution of the vertical
207 component waveform from the radial and transverse waveforms with a central frequency of ~1 Hz. This
208 frequency was selected on account of significant source energy detected in the ~1 Hz range of teleseismic *P*
209 arrivals, which are sensitive to crustal-scale anomalies. It also provides a favourable lateral sensitivity with
210 respect to Fresnel zone width (~15 km at Moho depth) when the conversions from *P* to *S* are mapped as
211 velocity and crustal thickness variations.

212 The complete set of 1765 events (Fig. 3) and 32 stations produced 21,671 preliminary RFs. These RFs were
213 manually inspected using the FuncLab trace editor and a subset of 9,674 RFs were selected for further analysis
214 using the visual clarity of the direct arrivals as an acceptance criterion. Due to high noise levels and fewer
215 events associated with the temporary BASS array dataset, a modest number of good quality RFs resulted from
216 the above selection method, so different selection criteria were applied that assessed the *P*-arrival, Moho
217 conversion and later amplitudes in conjunction with overall noise levels exhibited by the transverse component
218 RFs. This enabled the temporary BASS stations to yield between 2 and 30 good quality receiver functions, and
219 increased the number of stations where H-κ stacking and NA inversion could be applied from 13 to 20.

220 **5.2 *H-κ* stacking**

221 Having obtained reliable *P*-wave RFs, the *H-κ* stacking technique is used to estimate crustal thickness and bulk
222 *Vp/Vs* for individual stations. We apply the method of Zhu and Kanamori (2000) to stations where the direct *Ps*
223 (Moho *P*-to-*S* conversion) phase and its multiples are observed. This technique makes use of a grid search to
224 determine the crustal thickness (*H*) and *Vp/Vs* (*κ*) values that correspond to the peak amplitude of the stacked

225 phases. A clear maximum requires a contribution from both the primary phase (*Ps*) and the associated multiples
226 (*PpPs* and *PpSs+PsPs*). In the absence of multiples, the maximum becomes smeared out due to the inherent
227 trade-off between crustal thickness (*H*) and average crustal velocity properties (*κ*) (Ammon et al., 1990; Zhu and
228 Kanamori, 2000). The *H-κ* stacking algorithm reduces the aforementioned ambiguity by summing RF
229 amplitudes for *Ps* and its multiples - *PpPs* and *PpSs+PsPs* - at arrival times corresponding to a range of *H* and
230 *Vp/Vs* values. In the *H-κ* domain the equation for stacking amplitude is

$$s(H,\kappa) = \sum_{j=1}^{N} w_1 r_j(t_1) + w_2 r_j(t_2) + w_3 r_j(t_3)$$

231 (1)

232 where $r_j(t_j)$; i=1,2,3 are the RF amplitude values at the expected arrival times t_1, t_2, t_3 of the *Ps*, *PpPs*,
233 *PpSs+PsPs* phases respectively for the jth RF, w_1, w_2, w_3 are weights based on the signal to noise ratio
234 ($w_1+w_2+w_3$=1), and *N* is the total number of radial RFs for the station. $s(H,\kappa)$ achieves its maximum value when
235 all three phases stack constructively, thereby producing estimates for *H* and *Vp/Vs* beneath the station (see
236 Figure 5 and Supplementary Figures S1-S4). In this study, the weighting factors used are w_1=0.6, w_2=0.3,
237 w_3=0.1. The *H-κ* approach requires an estimate of the mean crustal *P*-wave velocity, which is used as an initial
238 value. Based on the results of a previous seismic refraction study (Drummond and Collins, 1986), we use an
239 average crustal velocity of *Vp* = 6.65 km/s to obtain our estimates of *H* and *κ* in the study area, noting that *H-κ*
240 stacking results are much more dependent on *Vp/Vs* than *Vp* (Zhu and Kanamori, 2000). To estimate the
241 uncertainties in the *H-κ* stacking results, we compute the standard deviation of the *H* and *κ* values at each
242 station. When only a small number of RFs are available at a station (e.g. 4 in the case of MILA) the estimates
243 are unlikely to be particularly robust, and in such instances are perhaps best viewed as a lower bounds on
244 uncertainty.

245 While simple to implement, the Zhu and Kanamori (2000) method can suffer from large uncertainties due to its
246 assumption of a simple flat-laying layer over a half-space with constant crustal and upper mantle properties.
247 Consequently, there are only two search parameters (*H* and *κ*) plus *a priori* information (*Vp*, weightings) and it
248 does not account for variation with backazimuth. These problems can cause non-unique and inaccurate
249 estimates, which can lead to potentially misleading interpretations; for instance, a low velocity upper crustal
250 layer can appear as a very shallow Moho in an *H-κ* stacking search space diagram. Also, a dipping Moho and/or
251 anisotropic layers within the crust can contribute to uncertainty.

252 **5.3 Nonlinear waveform inversion**

253 In an effort to refine the crustal model, we invert a stack of the radial RFs by adopting the workflow described
254 by Shibutani et al. (1996). We divide the waveform data (RFs) into four 90° quadrants based on the backazimuth
255 of their incoming energy. The 1ˢᵗ quadrant backazimuth range is from 0° and 90°, and an equivalent range in a
256 clockwise direction defines the consecutive quadrants. The 2ⁿᵈ and 3ʳᵈ quadrants (south-eastern and south-
257 western backazimuths) have very small numbers of RFs. Data from the 1ˢᵗ and 4ᵗʰ quadrants are of better quality,
258 with the 1ˢᵗ quadrant showing more coherency than the 4ᵗʰ quadrant, which is likely due to the orientation of
259 surrounding tectonic plate boundaries and hence the pattern of *P*-wave energy radiated towards Australia.

260   Kennett and Furumura (2008) showed that seismic waves arriving in Australia from the northern azimuths
261   undergo multiple scattering but low intrinsic attenuation due to heterogeneity in the lower crust and mantle; this
262   tends to produce prolonged high-frequency coda. An important assumption in our inversion is that we neglect
263   anisotropy and possible Moho dip, which we assume have a second order influence on the waveforms we use to
264   constrain 1-D models of the crust and upper mantle.

265   Visual examination of coherency in *P* to *S* conversions allows us to select a subset of RF waveforms for
266   subsequent stacking. This resulted in groups of mutually coherent waveforms after which a moveout correction
267   is then applied to remove the kinematic effect of different earthquake distances prior to stacking using a cross-
268   correlation matrix approach described in Chen et al. (2010) and Tkalčić et al. (2011). Our visual acceptance
269   criteria yields RFs at only 14 out of the 32 stations used for this study. An example of some stacked RFs is
270   given in Figure 4.

271   We invert RFs for 1-D seismic velocity structure beneath selected seismic stations using the Neighbourhood
272   Algorithm or NA (Sambridge, 1999a,b) in order to better understand the internal structure of the crust and the
273   nature of the transition to the upper mantle. NA makes use of Voronoi cells to help construct a searchable
274   parameter space, with the aim of preferentially sampling regions of low data misfit. In the inversion process, a
275   Thomson-Haskell matrix method (Thomson, 1950 and Haskell, 1953) was used to calculate a synthetic radial
276   RF for a given 1-D (layered) structure. During the inversion, as in Shibutani et al. (1996) and Clitheroe et al.
277   (2000), each model is described by six layers: a layer of sediment, a basement layer, an upper crust, middle crust
278   and lower crust, and an underlying mantle layer, all of which feature velocity gradients and potentially, velocity
279   jumps across boundaries. The inversion involves constraining 24 parameters: *Vs* values at the top and bottom of
280   each layer, layer thickness and the *Vp/Vs* ratio in each layer (Table 1). The inclusion of *Vp/Vs* ratio as an
281   unknown primarily aims to accommodate the effects of a sediment layer with limited prior constraints
282   (Bannister et al., 2003). There are two important controlling parameters required by NA: (1) the number of
283   models produced per iteration (n_s); and (2) the number of neighbourhoods re-sampled per iteration (n_r). After a
284   number of trials we chose the maximum number of iterations to be 5500, with n_s=13 and n_r=13 for all iterations.
285   We employ a chi-squared χ^2 metric (see Sambridge 1999a for more details) to compute the misfit function,

286   which is a measure of the inconsistency between the true ϕ_i^{obs} , and predicted, $\phi_i^{pre}(m)$ waveforms for a
287   given model *m* :

$$\chi_v^2(m) = \frac{1}{v} \sum_{i=1}^{N_d} \left(\frac{\phi_i^{obs} - \phi_i^{pre}(m)}{\sigma_i} \right)$$

288   (2)

289   where σ_i represents the noise standard deviation determined from ϕ_i^{obs} , following the method described in
290   Gouveia and Scales (1998), and v represents the number of degrees of freedom (the difference between the
291   number of observations and the number of parameters being inverted for). Using the above stated parameters,
292   the inversion targets the 1-D structure that produces the best fit between the predicted and observed RF. Figures

293 7-9 and Supplementary Figures S5-S9 present example results of inversions via density plots of the best 1000

294 data-fitting *S*-wave velocity models produced by the NA. The optimum data fitting model is plotted in red.

6 Results

6.1 *H-κ* stacking results

297 Maps of crustal thicknesses and average *Vp/Vs* from H-κ stacking in southeast Australia from 16 stations are

298 shown in Figure 6. At the remaining stations, we could not detect any clear multiples or Moho conversions in

299 the RFs from any direction. A previous study by Chevrot and van der Hilst (2000) has noted that this region is

300 devoid of clear multiples. The crustal thickness for all analysed stations in the study area varies from 23.2 ± 5.0

301 km (BA02) beneath NW Tasmania to 39.1 ± 0.5 km (CAN) beneath the Lachlan Fold Belt, and the variation

302 strongly correlates with topography. Crust beneath VanDieland (Fig. 6a) is thin in the north (~37.5 km) and

303 south (~33 km), but appears to be considerably thinner beneath the Victorian and Tasmanian margin of Bass

304 Strait (~25 km). The mountainous region of the Lachlan Fold Belt has the deepest Moho at 39.1 ± 0.5 km

305 (CAN) and a corresponding *Vp/Vs* value of 1.73 ± 0.02. Crust that is consistently between ~31 and 33 km thick

306 lies beneath the East Tasmania Terrane and Eastern Bass Strait (ETT+EB). *Vp/Vs* ratio varies between ~1.65

307 beneath station BA11, which also exhibits the thinnest crust, and ~1.93 beneath stations BA19 and BA20 in

308 southern Victoria. There is no obvious correlation between the number of RFs used in the H-κ stacking and the

309 size of the uncertainty in either Moho depth or *Vp/Vs*, but as mentioned previously, the uncertainty estimates

310 for stations with a low number of RFs are likely to be less robust. Table 2 shows a summary of *H-κ* stacking

311 results for the stations that have been analysed.

6.2 Nonlinear inversion results

313 Results of the NA inversion were successfully obtained for a selection of permanent and temporary stations, as

314 shown in Table 2 and Figure 10. If the Moho is defined by a gentle velocity gradient, the base of the velocity

315 gradient is used as a proxy for the Moho depth, as done in previous RF (e.g. Clitheroe et al., 2000; Fontaine et

316 al., 2013a) and seismic refraction (Collins, 1991; Collins et al., 2003) studies. We also adopt an upper mantle

317 velocity of Vp = 7.6 km/s (i.e. Vs = 4.3-4.4 km/s for *Vp/Vs* ratios of 1.73-1.77 at the base of the Moho gradient)

318 following Clitheroe et al. (2000) who used this value for RF studies, and Collins et al. (2003) who used Vp > 7.8

319 km/s for their summary of both seismic refraction and RF results; these Vp values are consistent with global

320 Earth models (e.g. Kennett et al., 1995). Therefore, we also require the *S*-wave velocity to be >~4.4 km/s

321 beneath the Moho. We present the *S*-wave velocity profiles from the NA inversion for stations CAN, MOO,

322 TOO, YNG, BA13 and BA17 in Figures 7-9, together with observed and predicted RFs. The *S*-wave velocity

323 inversion results of the remaining stations are included as supplementary material (see Supplementary Figures

324 S5-S8). In assigning the Moho depth, we consider three criteria to examine the quality of the inversion result:

325 (1) misfit value χ^2 ; (2) the quality of the RF stack (which is based on our ability to pick the direct and multiple

326 phases); and (3) the visual fit between the synthetic and observed RF. Models that fail to fit significant arrivals

327 in the observed RF are rejected. Based on these criteria, the inversion results are classified as:

328 • Very good: very low χ^2 (typically < 0.4), very good visual fit to direct and multiple phases.

- Good: low χ^2 (typically 0.4-0.8), direct phases clearly visible, multiple phases less clear, and a good visual fit to all major identifiable phases.

- Poor: medium to high χ^2 (in the range 0.8-1.2), direct phases visible, multiple phases unclear, and moderate visual fit to some identifiable phases.

In general, the optimum χ^2 value is normally considered to be 1, since below this value, the tendency is to fit noise rather than signal. However, this is for the ideal case when the number of degrees of freedom and the absolute values of the data uncertainty are well known (e.g. in the case of a synthetic test). In the case of observational data, these values are often poorly constrained, so using the relative χ^2 values coupled with visual assessment of the data fit appears to be reasonable. With regard to the character of the crust-mantle transition, this study classifies the transition zone as sharp ≤ 2 km, intermediate 2-10 km or broad ≥ 10 km as initially proposed by Shibutani et al. (1996) and modified by Clitheroe et al. (2000).

We note that for the seven permanent stations for which we produce receiver function inversion/H-κ stacking results, five have estimates of Moho depth from previous receiver function studies. Clitheroe et al., (2000) estimated Moho depth at 49 km beneath CAN based on a non-linear inversion, which is ~10 km greater than the results we obtain for both NA inversion and H-κ stacking (see section 7.1 for further discussion of this discrepancy). Ford et al. (2010) determine Moho depth beneath stations MOO, TOO, TAU and YNG using H-κ stacking and find values (compared to our H-κ stacking results) of 33±3 km (33.0±1.2 km), 34±3 km (37.5±1.2 km), 32±3 km (33.5±1.9 km) and 33±2 km (37.3±0.5 km) respectively. These are all within error, with the slight exception of station YNG, located in Young, on the western flanks of the Great Dividing Range, where we might expect the crust to be slightly thicker than average. Overall, however, these similarities suggest that our results are likely to be robust.

7 Discussion

For convenience, the seismic stations are separated into three groups (Fig. 2) based on tectonic setting and the results obtained. Stations YNG, CAN, CNB, MILA and BA13 are located in the Lachlan Fold Belt; stations BA02, BA11, BA19, BA20, TAU, MOO and TOO sit above the VanDieland microcontinental block; and stations BA07, BA08, BA09 and BA17 lie in the East Tasmania Terrane and Eastern Bass Strait (ETT+EB). Stations BA22 and BA24 lie to the west of VanDieland. This discussion focuses on crustal thickness, the nature of the Moho and crustal velocity and velocity ratio variations from *H-κ* stacking and the 1-D *S*-wave velocity models. Overall, the agreement between Moho depths obtained from the H-κ stacking results and NA-inversion is generally within error (Table 2), which makes a joint interpretation more straight forward. Comparison is also made to other studies that have examined crustal seismic properties in southeast Australia, and we attempt to integrate our new findings with previous results from teleseismic tomography, SKS splitting and ambient noise tomography in order to better understand the crust and upper mantle structure and dynamics beneath this region.

7.1 Lateral variation of crustal thickness and nature of the Moho

The RF analysis clearly reveals the presence of lateral changes in crustal thickness that span mainland Australia

through Bass Strait to Tasmania (Figures 6 and 10; in the latter case, RF depths from previous studies are also included for reference). The stations located in the Palaeozoic Lachlan Fold Belt reveal a generally thick crust that ranges between ~37 and 40 km. Although the Moho was picked as a velocity jump for stations YNG, CAN and CNB, the velocity nonetheless tends to continue to increase with depth below the discontinuity. This, coupled with the fact that Clitheroe et al. (2000) estimate the Moho to be almost 10 km deeper beneath CAN, is consistent with the presence of mafic underplating (e.g. Drummond and Collins, 1986; Shibutani et al., 1996; Clitheroe et al., 2000), sourced from the ambient convecting mantle. The top and bottom of such a layer could feature a velocity step with depth and its internal structure is likely to be layered and/or gradational, hence resulting in uncertainty in the true Moho depth. Based on deep crustal reflection profiling, Glen et al. (2002) suggested that the deep Moho underlying the Lachlan Orogen results from magmatic underplating that added a thick Ordovician mafic layer at the base of the crust coupled with a thick sequence of Ordovician mafic rocks that can be found in the mid and lower crust. Finlayson et al. (2002) and Glen et al. (2002) also inferred the presence of underplating near CNB and CAN from seismic refraction data. Collins (2002) postulated that the underplating might have occurred in the back-arc region of a subduction zone due to pronounced adiabatic decompression melting in the asthenosphere. The seismic tomography model of Rawlinson et al. (2010, 2011) exhibits an increase in P-wavespeed at 50 km depth beneath CAN, CNB and YNG and the authors suggest that magmatic underplating may be the cause of the high velocity anomaly. A recent study by Davies et al. (2015) identified the longest continental hotspot track in the world (over 2000 km total length), which began in north Queensland at ~33 Ma, and propagated southward underneath the present-day Lachlan Fold Belt and Bass Strait. The magmatic underplating could therefore be a consequence of the passage of the continent above a mantle upwelling leading to a more diffuse crust-mantle transition zone. The thickened crust and a transitional Moho observed in the Lachlan Fold Belt are consistent with the proposed delamination models of Collins and Vernon (1994).

Strong lateral changes in crustal seismic structure (Figures 6 and 10) beneath VanDieland appear to be a reflection of the region's complex tectonic history. The thick crust (~37 km) beneath the Selwyn Block (see Figure 1 for its location) – within the northern margin of VanDieland in southern Victoria – thins dramatically to ~26 km as it enters Bass Strait, increases to ~30 km beneath King Island (BA11), then thins to ~23 km beneath NW Tasmania, before increasing to ~33 km in southern Tasmania. The results in southern Tasmania agree with those of Korsch et al. (2002) from a seismic reflection profile adjacent to the seismic stations TAU and MOO. The thinner crust beneath Bass Strait and its margins may be a consequence of lithospheric thinning and/or delamination associated with failed rifting that accompanied the break-up of Australia and Antarctica (Gaina et al., 1998). Stations BA07, BA08, BA09 and BA17 (ETT+EB) collectively indicate crust of relative uniform thickness (∼31-32 km, Figures 10a,b). Relative to western Bass Strait, the crust is slightly thicker in this part of the study area, which may suggest underplating associated with a Palaeozoic subduction system (e.g. Drummond and Collins, 1986; Gray and Foster, 2004).

In general, our understanding of crustal thickness variations are limited by station separation, so it is difficult to determine whether smooth variations in thickness or step-like transitions explain the observations.

7.2 *Vp/Vs* and bulk crustal composition

402 *Vp/Vs* can constrain chemical composition and mineralogy more robustly than *P*- or *S*-wave velocity in isolation
403 (Christensen and Fountain, 1975). We observe variations in *Vp/Vs* across the study region, which we can largely
404 equate with variations in composition or melt. Studies in mineral physics and field observations show (1) an
405 increase in *Vp/Vs* with decreasing SiO_2 content in the continental crust (Christensen, 1996) and (2) partial melt
406 is revealed by elevated *Vp/Vs*, especially if the anomaly is localised to an intra-crustal layer (Owens and Zandt,
407 1997). A more felsic (SiO_2) composition in the lower crust is represented by a lower *Vp/Vs,* which reflects
408 removal of an intermediate-mafic zone by delamination, whereas a more mafic lower crust is revealed by higher
409 *Vp/Vs* (> 1.75) which may be due to underplated material (Pan and Niu, 2011). However, lower crustal
410 delamination can also result in decompression melting, which can yield elevated *Vp/Vs* (He et al., 2015). We
411 interpret the variation of observed *Vp/Vs* in the southern Tasmanides to be a consequence of compositionally
412 heterogeneous crust and localised partial melt that may likely be sourced from recent intraplate volcanism
413 (Rawlinson et al., 2017).

414 Figure 6b shows the distribution of bulk *Vp/Vs* across the study area. The pattern of *Vp/Vs* ratios appears to
415 delineate three distinct zones of crust. Beneath the Lachlan Orogen, values are ~1.75, which is consistent with
416 the presence of a mafic lower crust, as suggested by a number of other studies (Drummond and Collins, 1986;
417 Shibutani et al., 1996; Clitheroe et al., 2000; Finlayson et al., 2002). Beneath eastern Bass Strait, the *Vp/Vs*
418 ratios are slightly lower, with BA07, BA08 and BA09 exhibiting values of 1.70, 1.70 and 1.71 respectively.
419 These values are in agreement with constraints from seismic reflection and refraction studies (Finlayson et al.,
420 2002; Collins et al., 2003) and may indicate a felsic to intermediate crustal composition. The geology of
421 Flinders Island, which hosts both BA07 and BA08, is dominated by Devonian granites, which is consistent with
422 this observation. Beneath VanDieland, *Vp/Vs* is highly variable, with the greatest contrast between BA11
423 (~1.65) and BA19/20 (~1.93), and BA19/20 and TOO (1.68). BA11 is located on King Island, which is
424 characterised by Precambrian and Devonian granite outcrops, which may help explain the low *Vp/Vs*. The high
425 *Vp/Vs* beneath BA19/20 is harder to explain, but could be caused by melt in the crust associated with the Newer
426 Volcanics Province, which sits along the Cosgrove intraplate volcanic track, and last erupted only ~4.6 ka
427 (Rawlinson et al., 2017). The return to lower *Vp/Vs* beneath TOO over a relatively short distance (~100 km) is
428 also difficult to explain, but we note that this region of Victoria is underlain by granite intrusions.

429 In summary, the crust beneath VanDieland exhibits the greatest lateral heterogeneity in *Vp/Vs*, which likely
430 reflects considerable variations in composition and the presence of melt. This can partially be explained by the
431 tectonic history of the region, which includes failed rifting in Bass Strait accompanied by widespread magma
432 intrusion and granite emplacement, and more recently, the passage of a plume (Rawlinson et al., 2017).
433 Furthermore, Moore et al. (2015) used reflection transects and potential field data to infer that VanDieland is
434 comprised of up to seven continental ribbon terranes that are bounded by major faults and suture zones, which
435 were likely amalgamated by the end of the Proterozoic. Hence, considerable variations in composition and
436 hence *Vp/Vs* ratio are to be expected.

437 **7.3 Moho depth comparison**

438 Prior to this study, a variety of seismic methods have been used to constrain Moho depth in southeast Australia,
439 including receiver functions, reflection profiling and wide-angle refection and refraction experiments. In an

440 effort to combine the results from all of these studies into a single synthesis, Kennett et al., (2011) developed the
441 AusMoho model. This included Moho depth estimates from over 11,000 km of reflection transects across the
442 continent, numerous refraction studies, and 150 portable and temporary stations. Due to irregular sampling, the
443 detail of this model is highly variable; for example, the region beneath Bass Strait is constrained by only five
444 measurements, whereas the central Lachlan Fold Belt around Canberra (see Figure 1 for location) features
445 relatively dense sampling at ~50 km intervals or less.

446 AusMoho includes previous receiver function results from Shibutani et al. (1996), Clitheroe et al. (2000),
447 Fontaine et al. (2013a) and Tkalcic et al (2012), as well as reflection and refraction transects in Tasmania, parts
448 of the Lachlan Orogen, and western Victoria. Figure 11 illustrates AusMoho for our study region, which
449 exhibits large variations in Moho depth (from ~10 km to >50 km). These extremes are due to the presence of
450 oceanic crust outboard of the passive margin of the Australian continent, and the root beneath the Southern
451 Highlands, which represent the southern extension of the Great Dividing Range in New South Wales.
452 Superimposed on Figure 11 are Moho depths from the four previous receiver function studies cited above, plus
453 NA inversion and H-κ depth estimates from this study. As expected, the correlation between the previous RF
454 results and AusMoho is generally good, since they were part of the dataset used to build this model. In places
455 where they don't match, this can be attributed to the presence of seismic refraction or reflection lines which
456 were also used to constrain AusMoho.

457 In general, the agreement between the results from this study and AusMoho is good, but there are exceptions.
458 For instance, CAN, CNB, YNG and MILA tend to be somewhat shallower than AusMoho. However, this can be
459 attributed to the likely presence of mafic underplating alluded to earlier, which can effectively yield two options
460 for the Moho transition due to an expected high (>1.85) Vp/Vs in the underplate layer (e.g. Cornwell et al.,
461 2010). AusMoho Moho depths beneath BA07 and BA08 are considerably shallower than our estimates, which
462 we attribute to a lack of data coverage in this region. Sizeable discrepancies also exist beneath BA02, BA19 and
463 BA20; in the former case, the uncertainty in our H-κ stacking estimate is 5 km, which may be a factor here. In
464 the latter case, we also note that there is sparse data coverage southeast of Melbourne to constrain AusMoho, so
465 it would appear that our new Moho depths are more likely to be correct. Overall, while there is good consistency
466 between AusMoho and our new results, any updated version of AusMoho should incorporate the Moho depth
467 estimates from this study.

468 Although AusMoho did make use of results from a 3-D wide-angle reflection and refraction survey of Tasmania
469 (offshore shots and on-shore stations), it only used a few sample points for the final Moho model (Kennett et al.,
470 2011), and therefore the resolution of AusMoho is considerably less than the Moho model produced by
471 Rawlinson et al. (2001). Consequently, we plot our three RF results on top of this model in Supplementary
472 Figure S10. The agreement between the Moho model and RF depths beneath MOO and TAU is good, but RF
473 estimates beneath BA02 are shallower than the Moho model by about 4 km. However, this is within the margin
474 of error for the H-κ stacking result.

475 **7.4 Synthesis**

476 In this final section, we present a synthesis of results for southeast Australia that are based on: (1) our new

477 receiver function results; (2) teleseismic SKS splitting results from Bello et al. (2019a); (3) teleseismic
478 tomography undertaken by Bello et al. (2019b); (4) ambient noise crustal imaging results from Young et al.
479 (2013); and (5) AusMoho (Kennett et al., 2011). This synthesis is encapsulated in the plot shown in Figure 12,
480 which is a representative transect through the Lachlan Orogen south through Bass Strait and into Tasmania.
481 Moho depths are taken from AusMoho, and refined where additional information is available from our new RF
482 results; crustal P-wave velocity is taken from the ambient noise results (following conversion from *S*-wave
483 velocity – see Bello et al, 2019b for more details); and mantle *P*-wave velocities are taken from Bello et al,
484 (2019b). Arrows are based on interpreted mantle flow patterns undertaken as part of the shear wave splitting
485 study. This previous study used approximately the same temporary and broadband station network that was used
486 in the current study, and found that beneath the Lachlan Orogen, fast axis orientations of anisotropy were
487 aligned with contemporary plate motion (NNE), but beneath Bass Strait, a radial pattern was observed that is
488 consistent with an upwelling mantle that impinges on the lithosphere and spreads out in all directions.
489 Interestingly, the location of this phenomenon corresponds approximately to the predicted location of the
490 Cosgrove hotspot track source (Davies et al., 2015), and may be caused by an upwelling mantle plume. Thus,
491 the low velocities in the upper mantle beneath Bass Strait may be due to elevated temperatures and melt,
492 although it is not straightforward to explain the higher velocities below 200 km depth in this context.

493 The thicker Moho boundary beneath the Lachlan Orogen (Figure 12) reflects the likely presence of
494 underplating, which makes the base of the crust harder to discern seismically. However, the crust is clearly
495 thicker here than beneath Bass Strait or Tasmania. Moho depth beneath the northern part of the Figure 12 is not
496 constrained by our RF results, but according to AusMoho, it is relatively flat, which is consistent with
497 Precambrian crust, and there is a faster mantle lithosphere. The strong variations in crustal velocity beneath Bass
498 Strait can be attributed to failed rifting resulting in the formation of thick (>10 km) sedimentary basins and
499 elevated temperatures (lower velocities), and intrusion of mafic rich material into the lower and mid crust
500 (higher velocities).

501 **8 Conclusions**

502 We used *H-κ* stacking of teleseismic RFs to determine crustal thickness and *Vp/Vs* ratio and generate 1-D *S*-
503 wave velocity profiles of the crust from RF inversion in order to investigate the internal crustal velocity
504 structure beneath the southern Tasmanides in southeast Australia. Our main findings are summarised below.

505 • The thick crust and broad crust-mantle transition beneath the Lachlan Fold Belt may be caused by
506 magmatic underplating of mafic materials beneath the crust, which is consistent with an elevated *Vp/Vs*
507 ratio (relative to ak135) of ~1.73. Thicker crust is also to be expected from the elevated topography of
508 the eastern Lachlan Fold Belt.

509 • The crustal structure is complex beneath VanDieland. It thins considerably from the northern tip of the
510 microcontinent (~37 km) into Bass Strait (~26 km) and northern Tasmania (~23 km), yet in southern
511 Tasmania the crust is somewhat thicker (~33 km) compared to Bass Strait. This may in part be due to
512 the complex origins of the microcontinent, which appears to be comprised of multiple Precambrian
513 continental ribbons, but is also likely due to failed rifting in Bass Strait before and during the

14

separation of Australia and Antarctica. This resulted in lithospheric stretching/delamination, magmatic intrusion, and the deposition of thick sedimentary sequences. Recent intraplate volcanism and the possible progression of a mantle plume beneath VanDieland in the last few thousand years may also have produced compositional heterogeneity and melt in the crust. Such events are likely to contribute significantly to variations in crustal thickness and the pronounced changes in *Vp/Vs* that we observe.

- Stations within the ETT+EB collectively indicate crust of uniform thickness ($\sim$31-32 km) and uniform *Vp/Vs* ($\sim$1.70), which clearly distinguishes it from VanDieland. This region of the crust likely represents a southern continuation of the Lachlan Orogen, and therefore is underpinned by crust of oceanic origin.

- Comparison of our new Moho depth results with the AusMoho model reveals an overall consistency, although at some of our station locations where AusMoho has few constraints, there are noticeable differences, such as southern Victoria and beneath Flinders Island. The discrepancies beneath the Lachlan Orogen are attributed to the presence of underplated mafic material, which can obfuscate the location of the Moho.

- A synthesis of our new RF results with pre-existing teleseismic tomography, shear wave splitting and ambient noise studies reveals a complex lithosphere that has clearly been impacted by orogeny (thickened crust), failed rifting beneath Bass Strait (thinned crust and complex crustal velocities), and recent intraplate volcanism (high *Vp/Vs* ratios and a radial pattern of fast anisotropy patterns above a presumed zone of mantle upwelling).

9 Data availability

Dataset available at 10.6084/m9.figshare.12233723

10 Author contributions

M.B. performed the data analysis and wrote the draft manuscript. N.R and D.C. guided the study and assisted in interpretation. M.B., D.C. and N.R. discussed the results and revised the manuscript. A.R. and O.L. revised the manuscript and assisted with the interpretation.

11 Competing Interests: The authors declare no competing interests.

12 Acknowledgments

552

References

554 Amante, C. and Eakins, B. W.: ETOPO1 1 Arc-Minute Global Relief Model: Procedures, data sources and
555   analysis, NOAA technical memorandum NESDIS NGDC-24, 19pp, 2009.

556 Ammon, C. J.: The isolation of receiver effects from teleseismic P waveforms. Bull. Seis. Soc. Ame., 81, 2504–
557   2510, 1991.

558 Ammon, C. J., Randall, G., and Zandt, G.: On the nonuniqueness of receiver function inversions. J. Geophys.
559   Res., 95, 15 303–15 318, 1990.

560 Arroucau, P., Rawlinson, N., and Sambridge, M.: New insight into Cainozoic sedimentary basins and
561   Palaeozoic suture zones in southeast Australia from ambient noise surface wave tomography. Geophys. Res.
562   Lett., 37, http://dx.doi.org/10.1029/2009GL041974, 2010.

563 Bannister, S., Yu, J., Leitner, B., and Kennett, B. L. N.: Variations in crustal structure across the transition from
564   West to East Antarctica, Southern Victoria Land, Geophys. J. Int., 155, 870–884, 2003.

565 Bello, M., Cornwell, D. G., Rawlinson, N., and Reading, A. M.: Insights into the structure and dynamics of the
566   upper mantle beneath Bass Strait, southeast Australia, using shear wave splitting, Phys. Earth Planet. Inter.,
567   289, 45–62, https://doi.org/10.1016/j.pepi.2019.02. 002, 2019a.

568 Bello, M., Rawlinson, N., Cornwell, D. G., Crowder, E., Salmon, M., and Reading, A. M.: Structure of the crust
569   and upper mantle beneath Bass Strait, southeast Australia, from teleseismic body wave tomography, Phys.
570   Earth Planet. Inter., 294, https://doi.org/10.1016/j.pepi. 2019.106276, 2019b.

571 Berry, R. F., Steele, D. A., and Maffre, S.: Proterozoic metamorphism in Tasmania: implications for tectonic
572   reconstructions, Prec. Res., 166, 387–396. https://doi.org/10.1016/j. precamres.2007.05.004, 2008.

573 Bodin, T., Salmon, M., Kennett, B. L. N., and Sambridge, M.: Probabilistic surface reconstruction from multiple
574   datasets: an example for the Australian Moho, J. Geophys. Res.: Solid Earth, 117,
575   http://dx.doi.org/10.1029/2012JB009547, 2012a.

576 Bodin, T., Sambridge, M., Rawlinson, N., and Arroucau, P.: Transdimensional tomography with unknown data
577   noise, Geophys. J. Int., 189, 1536–1556, 2012b.

578 Boger, S. and Miller, J.: Terminal suturing of Gondwana and the onset of the Ross Delamerian Orogeny: the
579   cause and effect of an Early Cambrian reconfiguration of plate motions, Earth Planet. Sci. Lett., 219, 35–48,
580   2004.

581 Calvert, C. R. and Walter, M. R.: The Late Neoproterozoic Grassy Group of King Island, Tasmania: correlation
582   and palaeogeographic significance, Precam. Res., 100, 299–312, 2000.

583 Cawood, P. A.: Terra Australis Orogen: Rodinia breakup and development of the Pacific and Iapetus margins of
584   Gondwana during the Neoproterozoic and Palaeozoic. Earth-Science Reviews, 69, 249–279,
585   http://dx.doi.org/10.1016/j.earscirev.2004.09.001, 2005.

586 Cayley, R.: Exotic crustal block accretion to the eastern Gondwanaland margin in the Late Cambrian Tasmania,
587   the Selwyn Block, and implications for the Cambrian–Silurian evolution of the Ross, Delamerian, and
588   Lachlan orogens. Gond. Res., 19, 628–649. http://dx.doi.org/10. 1016/j.gr.2010.11.013, 2011a.

589   Cayley, R., Korsch, R. J., Moore, D. H., Costelloe, R. D., Nakamura, A., Willman, C. E., Rawlin, T. J., Morand,
590   V. J., Skladzien, P. B., and O'Shea, P. J.: Crustal architecture of central Victoria: results from the 2006 deep
591   crustal reflection seismic survey, Aust. J. Earth Sci., 59, 113–156, 2011b.

592   Chen, Y., Niu, F., Liu, R., Huang, Z., Tkalčić, H., Sun, L., and Chan, W.: Crustal structure beneath China from
593   receiver function analysis, J. Geophys. Res., 49(B033067), 2010.

594   Chevrot, S. and van der Hilst, R. D.: The Poisson ratio of the Australian crust: Geological and Geophysical
595   implications, Earth Planet. Sci. Lett., 183,121–132, 2000.

596   Christensen, N. I.: Poisson's ratio and crustal seismology, J. Geophys. Res., 101, 3139–3156, 1996.

597   Christensen, N. I. and Fountain, D. M.: Constitution of the lower continental crust based on experimental studies
598   of seismic velocities in granulite, Geol. Soc. Ame. Bull., 86, 227–236, 1975.

599   Clitheroe, G., Gudmundsson, O., and Kennett, B.: The crustal thickness of Australia, J. Geophys. Res., 105, 13
600   697–13 713, 2000.

601   Collins, C. D. N.: The nature of crust–mantle boundary under Australia from seismic evidence, In: Drummond
602   B. J. ed. The Australian lithosphere, Geol. Soc. Aust. Spec. Pub., 17, 67–80, 1991.

603   Collins, C. D. N., Drummond, B. J., and Nicoll, M. G.: Crustal thickness patterns in the Australian continent,
604   Geol. Soc. Ame. Spec. Papers, 372, 121–128, 2003.

605   Collins, W. J.: Nature of extensional accretionary origins, Tectonics, 21, 1024–1036, 2002.

606   Collins, W. J. and Vernon, R. H.: A rift–drift–delamination model of continental evolution: Palaeozoic tectonic
607   development of eastern Australia, Tectonophysics, 2(35), 1994.

608   Coney, P. J.: Plate tectonics and the Precambrian Phanerozoic evolution of Australia, PACRIM '95, Aust. Inst.
609   Mining and Metallurgy, pages 145–150, 1995.

610   Coney, P. J., Edwards, A., Hine, R., Morrison, F., and Windrim, D.: The regional tectonics of the Tasman
611   orogenic system, eastern Australia, J. Struct. Geol., 12(5/6), 519–543, 1990.

612   Cornwell, D. G., P. K. H. Maguire, R. W. England, and G. W. Stuart (2010), Imaging detailed crustal structure
613   and magmatic intrusion across the Ethiopian Rift using a dense linear broadband array, *Geochem. Geophys.*
614   *Geosyst.*, **11**, Q0AB03, doi:10.1029/2009GC002637.

615   Crowder, E., Rawlinson, N., Pilia, S., Cornwell, D. G., and Reading, A. M.: Transdimensional ambient noise
616   tomography of Bass Strait, southeast Australia, reveals the sedimentary basin and deep crustal structure
617   beneath a failed continental rift, Geophys. J. Int., 217, 970–987, 2019.

618   Davies, D. R., Rawlinson, N., Iaffaldano, N., and Campbell, I. H.: Lithospheric controls on magma composition
619   along Earth's longest continental hotspot track, Nature, 525, 511–514, 2015.

620   Drummond, B. J. and Collins, C. D. N.: Seismic evidence for underplating of the lower continental crust of
621   Australia, Earth Planet. Sci. Lett., 79, 361–372, 1986.

622   Drummond, B. J., Lyons, P., Goleby, B., and Jones, L.: Constraining models of the tectonic setting of the giant
623   Olympic Dam iron-oxide-copper-gold deposit, south Australia, using deep seismic reflection data,
624   Tectonophysics, 420, 91–103, 2006.

625   Eagar, K. C. and Fouch, M. J.: FuncLab: A MATLAB interactive toolbox for handling receiver function
626   datasets, Seismo. Res. Lett., https://doi.org/10.1785/gssrl.83.3.596, 2012.

627   Finlayson, D. M., Collins, C. D. N., and Denham, D.: Crustal structure under the Lachlan Fold Belt,
628   southeastern Australia, Phys. Earth Planet. Int., 21, 321–342, 1980.

629 Finlayson, D. M., Korsch, R. J., Glen, R. A., Leven, J. H., and Johnstone, D. W.: Seismic imaging and crustal
630   architecture across the Lachlan transverse zone, a crosscutting feature of eastern Australia, Aust. J. Earth
631   Sci., 49, 311–321, 2002.

632 Fishwick, S. and Rawlinson, N.: 3–D structure of the Australian lithosphere from evolving seismic datasets,
633   Aust. J. Earth Sci., 59, 809–826, 2012.

634 Foden, J., Elburg, M. A., Dougherty-Page, J., and Burtt, A.: The timing and duration of the Delamerian
635   Orogeny: correlation with the Ross Orogen and implications for Gondwana assembly, J. Geology, 114, 189–
636   210, 2006.

637 Fontaine, F. R., Tkalčić, H., and Kennett, B. L. N.: Crustal complexity in the Lachlan Orogen revealed from
638   teleseismic receiver functions, Aust. J. Earth Sci., 60, 413–430, 2013a.

639 Fontaine, F. R., Tkalčić, H., and Kennett, B. L. N.: Imaging crustal structure variation across southeastern
640   Australia, Tectonophysics, 582, 112–125, 2013b.

641 Foster, D. A. and Gray, D. R.: Evolution and structure of the Lachlan Fold Belt (Orogen) of eastern Australia,
642   Annu. Rev. Earth Planet. Sci., 28, 47–80, 2000.

643 Gaina, C., Müller, D., Royer, J. Y., Stock, J., Hardebeck, J., and Symonds, P.: The tectonic history of the
644   Tasman Sea, a puzzle with 13 pieces, J. Geophys. Res., 103,12,413–12,433,1998.

645 Gibson, G. M., Morse, M. P., Ireland, T. R., and Nayak, G. K.: Arc-continent collision and orogenesis in
646   western Tasmanides: insights from reactivated basement structures and formation of an ocean-continent
647   transform boundary off western Tasmania, Gondwana Res., 19, 608–627, 2011.

648 Glen, R. A.: The Tasmanides of Eastern Australia. In: Vaughan, A. P. M., Leat, P. T., Pankhurst, R. J. (Eds.),
649   Terrane Processes at the Margins of Gondwana, Geological Society, pages 23–96, 2005.

650 Glen, R. A.: Refining accretionary orogen models for the Tasmanides of eastern Australia, Aust. J. Earth Sci.,
651   60, 315–370, 2013.

652 Glen, R. A., Korsch, R. J., Direen, N. G., Jones, L. E. A., Johnstone, D. W., Lawrie, K. C., Finlayson, D. M.,
653   and Shaw, R. D.: Crustal structure of the Ordovician Macquarie Arc, eastern Lachlan Orogen, based on
654   seismic–reflection profiling, Aust. J. Earth Sci., 49, 323–348, 2002.

655 Glen, R. A., Percival, I. G., and Quinn, C. D.: Ordovician continental margin terranes in the Lachlan Orogen,
656   Australia: implications for tectonics in an accretionary orogen along the east Gondwana margin, Tectonics,
657   28, https://doi.org/:10.1029/2009TC002446, 2009.

658 Goldstein, P., Dodge, D., Firpo, M., and Minner, L.: SAC2000: Signal processing and analysis tools for
659   seismologists and engineers. Lee, W. H. K. and Kanamori, H. and Jennings, P. C. and Kisslinger, C. (Eds.).
660   In IASPEI International Handbook of Earthquake and Engineering Seismology, Academic Press, London,
661   2003.

662 Gouveia, W. P. and Scales, J. A.: Bayesian seismic waveform inversion: Parameter estimation and uncertainty
663   analysis, J. Geophys. Res., 103, 2759–2779, 1998.

664 Gray, D. R. and Foster, D. A.: Tectonic evolution of the Lachlan Orogen, southeastern Australia: historical
665   review, data synthesis and modern perspectives, Aust. J. Earth Sci., 51, 773– 817, 2004.

666 Gunn, P. J., Maidment, D. W., and Milligan, P.: Interpreting aeromagnetic data in areas of limited outcrop,
667   AGSO J. Aust. Geol. Geophys., 17, 175–185, 1997.

668 Harrington, B. et al (2004-2005). Inkscape. http://www.inkscape.org/.

669 Haskell, N. A.: The dispersion of surface waves in multilayered media, Bulletin of the Seismological Society
670   America, 43, 1734, http://dx.doi.org/10.1038/physci245109a0, 1953.

He, C. S., Santosh, M., Dong, S. W., and Wang, S. C.: Crustal thickning and uplift of the Tibetan Plateau inferred from receiver function analysis, J. Asian Earth Sci., 99,112–124, 2015.

Heintz, M. and Kennett, B. L. N.: Continental scale shear wave splitting analysis: Investigation of seismic anisotropy underneath the Australian continent, Earth Planet. Sci. Lett., 236, 106–119, 2005.

Kennett, B. L. N, Engdhal, E. R., and Buland, R.: Constraints on seismic velocities in the earth from travel times. Geophys. J. Int., 125, 228-248, 1995.

Kennett, B. L. N. and Furumura, T.: Stochastic waveguide in the lithosphere: Indonesian subduction zone to Australian craton, Geophys. J. Int., 172, 363–382, 2008.

Kennett, B. L. N., Salmon, M., Saygin, E., and Group, A.: AusMoho: the variation of Moho depth in Australia, Geophys. J. Int., 187, 946–958, 2011.

Korsch, R. J., Barton, T. J., Gray, D. R., Owen, A. J., and Foster, D. A.: Geological interpretation of a deep seismic reflection transect across the boundary between the Delamerian and Lachlan Orogens, in the vicinity of the Grampians, western Victoria, Aust. J. Earth Sci., 49, 1057–1075, http://dx.doi.org/10.1046/j.1440-0952.2002.00963.x, 2002.

Langston, C. A.: Structure under Mount Rainier, Washington, inferred from teleseismic body waves, J. Geophys. Res., 84, 4749–4762, https://doi.org/10.1071/EG994019, 1979.

Li, Z. X., Baillie, P. W., and Powell, C. M.: Relationship between northwestern Tasmania and East Gondwanaland in the Late Cambrian/Early Ordovician Paleomagnetic evidence, Tectonics, 16, 161–171, http://dx.doi.org/10.1029/96TC02729, 1997.

Ligorria, J. P. and Ammon, C. J.: Iterative deconvolution and receiver function estimation, Bull. Seism. Soc. Ame., 89, 1395–1400, 1999.

Moore, D., Betts, P. G., and Hall, M.: Fragmented Tasmania: the transition from Rodinia to Gondwana, Aust. J. Earth Sci., 62, 1–35, 2015.

Moore, D. H., Betts, P. G., and Hall, M.: Constraining the VanDieland microcontinent at the edge of East Gondwana, Australia, Tectonophysics, 687, 158–179, 2016.

Moresi, L., Betts, P. G., Miller, M. S., and Cayley, R. A.: Dynamics of continental accretion, Nature, 508, 245–248, 2014.

Morse, M., Gibson, G., and Mitchell, C.: Basement constraints on offshore basin architecture as determined by new aeromagnetic data acquired over Bass Strait and western margin of Tasmania, ASEG Extended Abstracts 2009, pages 1–9, http://dx.doi.org/10.1071/ASEG2009ab042, 2009.

Owens, T. J., Taylor, S. R., and Zandt, G.: Crustal structure at regional seismic test network stations determined from inversion of broadband teleseismic P waveforms, Bull. Seismo. Soc. Ame., 77, 631–632, 1987.

Owens, T. J. and Zandt, G.: Implications of crustal property with variations for models of Tibetan Plateau evolution, Nature, 387, 37–43, 1997.

Pan, S. Z. and Niu, F. L.: Large contrasts in crustal structure and composition between the Ordos plateau and the NE Tibetan plateau from receiver function analysis, Earth Plan. Sci. Lett., 303, 291–298, 2011.

Pilia, S., Arroucau, P., Rawlinson, N., Reading, A. M., and Cayley, R. A.: Inherited crustal deformation along the East Gondwana margin revealed by seismic anisotropy tomography, Geophys. Res. Lett., 43(23), 12082–12090, https://doi.org/10.1002/2016GL071201, 2016.

Pilia, S., Rawlinson, N., Cayley, R. A., Musgrave, R., Reading, A. M., Direen, N. G., and Young, M. K.: Evidence of micro–continent entrainment during crustal accretion, Sci. Rep., 5, http://dx.doi.org/10.1038/srep/08218, 2015a.

713 Pilia, S., Rawlinson, N., Green, N. G., Reading, A. M., Cayley, R., Pryer, L., Arroucau, P., and Duffet, M.:
714   Linking mainland Australia and Tasmania using ambient seismic noise tomography: Implications for the
715   tectonic evolution of the east Gondwana margin, Gond. Res., 28, 1212–1227, 2015b.

716 Porritt, S. W. and Miller, M. S.: Updates to FuncLab, a Matlab based GUI for handling receiver functions,
717   Computers and Geosciences, 111, 260–271, https://doi.org/10.1016/j. cageo.2017.11.022, 2018.

718 Rawlinson, N., Davies, D. R., and Pilia, S.: The mechanisms underpinning Cenozoic intraplate volcanism in
719   eastern Australia, Insights from seismic tomography and geodynamic modeling, Geophys. Res. Lett., 44(19),
720   9,681–9,690, 2017.

721 Rawlinson, N., Housman, G. A., Collins, C. D. N., and Drummond, B. J.: New evidence of Tasmania's tectonic
722   history from a novel seismic experiment, Geophys. Res. Lett., 28, 3337–3340, 2001.

723 Rawlinson, N. and Kennett, B.: Teleseismic tomography of the upper mantle beneath the southern Lachlan
724   Orogen, Australia, Phys. Earth Planet. Inter., 167, 84–97, http://dx.doi.org/ 10.1016/j.pepi2008.02.07, 2008.

725 Rawlinson, N., Kennett, B., Vanacore, E., Glen, R., and Fishwick, S.: The structure of the upper mantle beneath
726   the Delamerian and Lachlan orogens from simultaneous inversion of multiple teleseismic datasets, Gond.
727   Res., 19, 788–799, 2011.

728 Rawlinson, N., Kennett, B. L. N., Salmon, M., and Glen, R. A.: Origin of lateral heterogeneities in the upper
729   mantle beneath Southeast Australia from seismic tomography, Khan, A., and Deschamps, F. (Eds.), In The
730   Earth's Heterogeneous Mantle: A Geophysical, Geodynamical and Geochemical Perspective, pages 47–78,
731   Springer Geophysics, Springer, 2015.

732 Rawlinson, N., Pilia, S., Young, M., Salmon, M., and Yang, Y.: Crust and upper mantle structure beneath
733   southeast Australia from ambient noise and teleseismic tomography, Tectonophysics, 689, 143–156,
734   http://dx.doi.org/10.1016/j.tecto.2015.11.034, 2016.

735 Rawlinson, N., Pozgay, S., and Fishwick, S.: Seismic tomography: a window into deep Earth, Phys. Earth
736   Planet. Inter., 178, 101–135, 2010.

737 Rawlinson, N. and Urvoy, M.: Simultaneous inversion of active and passive source datasets for 3–D seismic
738   structure with application to Tasmania, Geophys. Res. Lett., 33, 2006.

739 Sambridge, M. S.: Geophysical inversion with a neighbourhood algorithm – I. Searching a parameter space,
740   Geophys. J. Int., 138, 479–494, 1999a.

741 Sambridge, M. S.: Geophysical inversion with a neighbourhood algorithm -II. Appraising the ensemble,
742   Geophys. J. Int., 138, 479–494, 1999b.

743 Saygin, E. and Kennett, B. L. N.: Ambient seismic noise tomography of Australian continent, Tectonophysics,
744   481, 116–125, http://dx.doi.org/10.1016/j.tecto.2008.11.013, 2010.

745 Shibutani, T., Sambridge, M. S., and Kennett, B. L. N.: Genetic algorithm inversion for receiver functions with
746   application to crust and uppermost mantle structure beneath Eastern Australia, Geophys. Res. Lett.,
747   23,1826–1832, 1996.

748 Spaggiari, C. V., Gray, D. R., and Foster, D. A.: Lachlan Orogen subduction–accretion systematics revisited,
749   Aust. J. of Earth Sci., 51, 549–553, 2004.

750 Spaggiari, C. V., Gray, D. R., Foster, D. A., and McKnight, S.: Evolution of the boundary between the western
751   and central Lachlan Orogen: implications for Tasmanide tectonics, Aust. J. Earth Sci., 50, 725–749, 2003.

752 Teasdale, J., Pryer, L., Stuart-Smith, P., Romine, K., Etheridge, M., Loutit, T., and Kyan, D.: Structural
753   framework and basin evolution of Australia's Southern Margin, APPEA J. Australian Petroleum Production
754   and Exploration Association, 43, 13–38, https://doi.org/10. 1785/0120030123, 2003.

755 Thomson, W. T.: Transmission of elastic waves through a stratified solid, J. of App. Phys., 21, 89-93, 1950.

756 Tkalčić, H., Chen, Y., Liu, R., Huang, H., Sun, L., and Chan, W.: Multi–step modelling of teleseismic receiver
757   functions combined with constraints from seismic tomography: Crustal structure beneath southeast China,
758   Geophys. J. Int., 187, 303–326, 2011.

759 Tkalčić, H., Rawlinson, N., Arroucau, P., and Kumar, A.: Multistep modelling of receiver-based seismic and
760   ambient noise data from WOMBAT array: crustal structure beneath southeast Australia, Geophys. J. Int.,
761   189, 1681–1700, https://doi.org/10.1111/j.1365-246X.2012.05442, 2012.

762 Wessel, P., Smith, W. H., Scharroo, R., Louis, J., and Wobbe, F.: Generic mapping tools: improved version
763   released, EOS Trans. Am. Geophys. Union, 94, 409-420, 2013.

764 Young, M. K., Cayley, R. A., McLean, M. A., Rawlinson, N., Arroucau, P., and Salmon, M.: Crustal structure
765   of the east Gondwana margin in southeast Australia revealed by transdimensional ambient seismic noise
766   tomography, Geophys. Res. Lett., 40, 4266–4271, 2013.

767 Young, M. K., Rawlinson, N., Arroucau, P., Reading, A., and Tkalčić, H.: High–frequency ambient noise
768   tomography of southeast Australia: new constraints on Tasmania's tectonic past, Geophys. Res. Lett., 38,
769   http://dx.doi.org/10.1029/2011GL047971, 2011.

770 Young, N., Tkalčić, H., Rawlinson, N., and Reading, A. M.: Full waveform moment tensor inversion in a low
771   seismicity region using multiple teleseismic datasets and ambient noise: application to the 2007 Shark Bay,
772   Western Australia, Earthquake. Geophys. J. Int., 188,1303–1321, https://doi.org/10.1111/j.1365-
773   246X.2011.05326, 2012.

774 Zhu, L. and Kanamori, H.: Moho depth variation in southern California from teleseismic receiver functions, J.
775   Geophys. Res., 105, 2969–2980, 2000.

776 **Table 1:** Model parameter bounds used in the Neighbourhood Algorithm receiver function inversion. V_s^{upper} and
777 V_s^{lower} represent the S-velocity at the top and bottom of a layer respectively. V_p/V_s represents P and S wave
778 velocity ratio within a layer.

Layer	Thickness (m)	V_s^{upper} (km/s)	V_s^{lower} (km/s)	V_p/V_s
Sediment	0-2	0.5-1.5	0.5-1.5	2.00-3.00
Basement	0-3	1.8-2.8	1.8-2.8	1.65-2.00
Upper crust	3-20	3.0-3.8	3.0-3.9	1.65-1.80
Middle crust	4-20	3.4-4.3	3.4-4.4	1.65-1.80
Lower crust	5-15	3.5-4.8	3.6-4.9	1.65-1.80
Mantle	5-20	4.0-5.0	4.0-5.0	1.70-1.90

779
780
781
782
783
784
785
786
787

788 **Table 2:** Summary of H-κ stacking and NA inversion results for the current study.

	Basic station information				Results				
Type	Station name	Lon (º)	Lat (º)	No of RFs	Moho Depth (km) (H-K stacking)	Bulk *Vp/Vs* (H-K stacking)	Moho Depth (km) (NA inversion)	Quality (NA inversion)	Moho type (NA inversion)
Temporary stations	BA02	145.20	-40.95	9	23.2±5.0	1.83±0.31	-	Moderate	Not evident
	BA03	145.84	-41.20	8	-	-	-	Moderate	Not evident
	BA07	148.31	-40.43	6	32.5±0.1	1.70±0.02	28	Good	Sharp
	BA08	147.97	-39.77	8	31.9±0.1	1.70±0.07	-	Poor	-
	BA09	147.32	-39.47	8	32.8±1.7	1.71±0.07	32	Good	Sharp
	BA11	143.98	-39.64	12	30.5±2.1	1.65±0.07	-	-	-
	BA13	148.83	-37.63	24	37.7±2.9	1.74±0.10	40	Good	Sharp
	BA17	146.33	-39.04	20	30.9±2.5	1.76±0.10	29	Good	Broad
	BA18	146.14	-38.02	3	-	-	38	Good	Sharp
	BA19	145.69	-38.57	20	25.5±2.4	1.93±0.14	-	Good	Not evident
	BA20	144.92	-38.42	30	26.3±1.6	1.93±0.12	29	Good	Sharp
	BA22	143.61	-37.99	5	-	-	29	Poor	Sharp
	BA24	142.54	-38.26	4	-	-	33	Poor	Sharp
Permanent stations	TAU	147.32	-42.91	41	33.5±1.9	1.70±0.08	33	Poor	Intermediate
	MOO	147.19	-42.44	58	33.0±1.2	1.71±0.04	34	Good	Sharp
	TOO	145.59	-37.57	276	37.5±1.2	1.68±0.04	36	Good	Sharp
	YNG	148.40	-34.20	178	37.3±0.5	1.76±0.04	35	Good	Sharp
	CAN	149.00	-35.32	402	39.1±0.5	1.73±0.02	40	Good	Sharp
	CNB	149.36	-35.32	155	38.5±1.1	1.70±0.04	39	Good	Broad
	MILA	149.16	-37.05	4	37.6±2.1	1.73±0.06	-	-	-

789

790

791

792

793
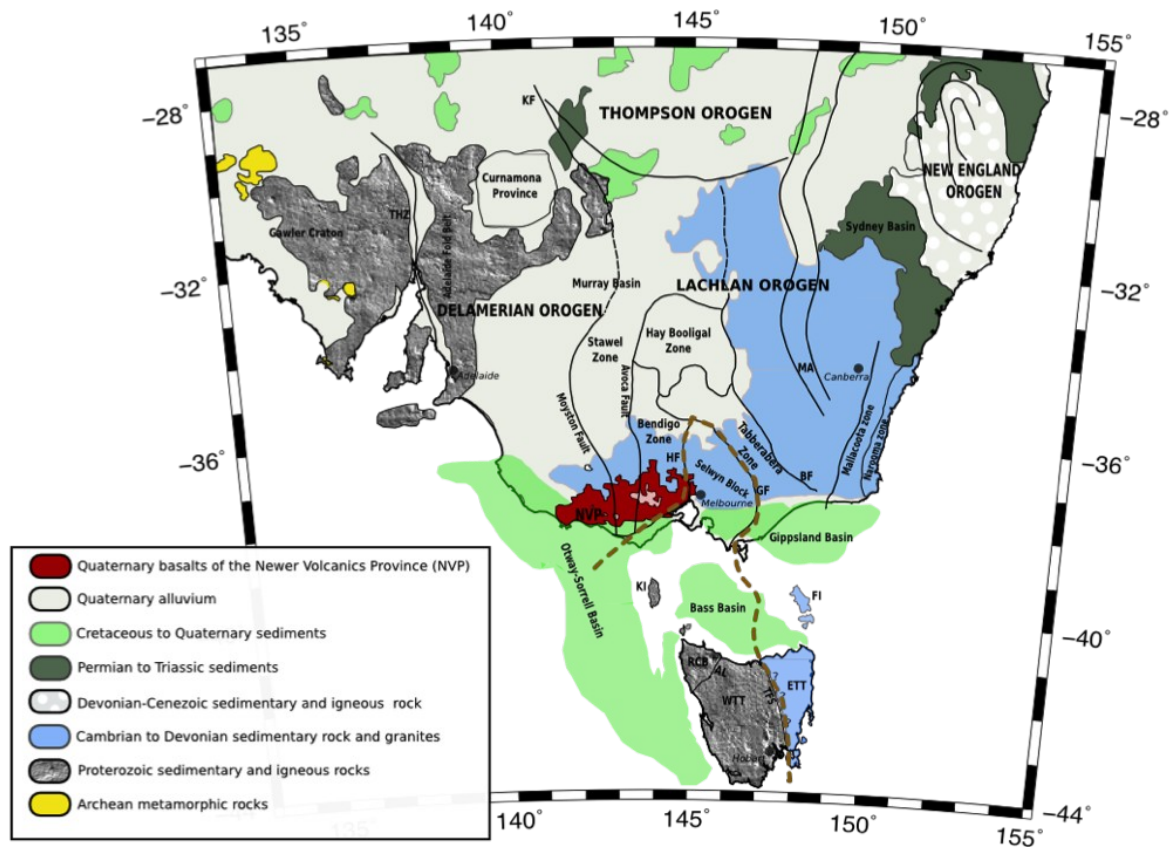
Figure 1: Regional map of southeastern Australia that shows key geological boundaries and the location of observed or inferred tectonic units (modified from Bello et al., 2019a). Thick black lines delineate structural boundaries and the thick brown dashed line traces out the boundary of VanDieland. HF = Heathcote Fault; GF = Governor Fault; BF = Bootheragandra Fault; KF = Koonenberry Fault; THZ = Torrens Hinge Zone; MA = Macquarie Arc, NVP = Newer Volcanics Province;; KI = King Island and FI = Flinders Island in Bass Strait; WTT = West Tasmania Terrane; ETT = East Tasmania Terrane; AL = Arthur Lineament; TFS = Tamar Fracture System and RCB = Rocky Cape Block. Outcrop boundaries are sourced from Rawlinson et al. 2016.

802

803

804
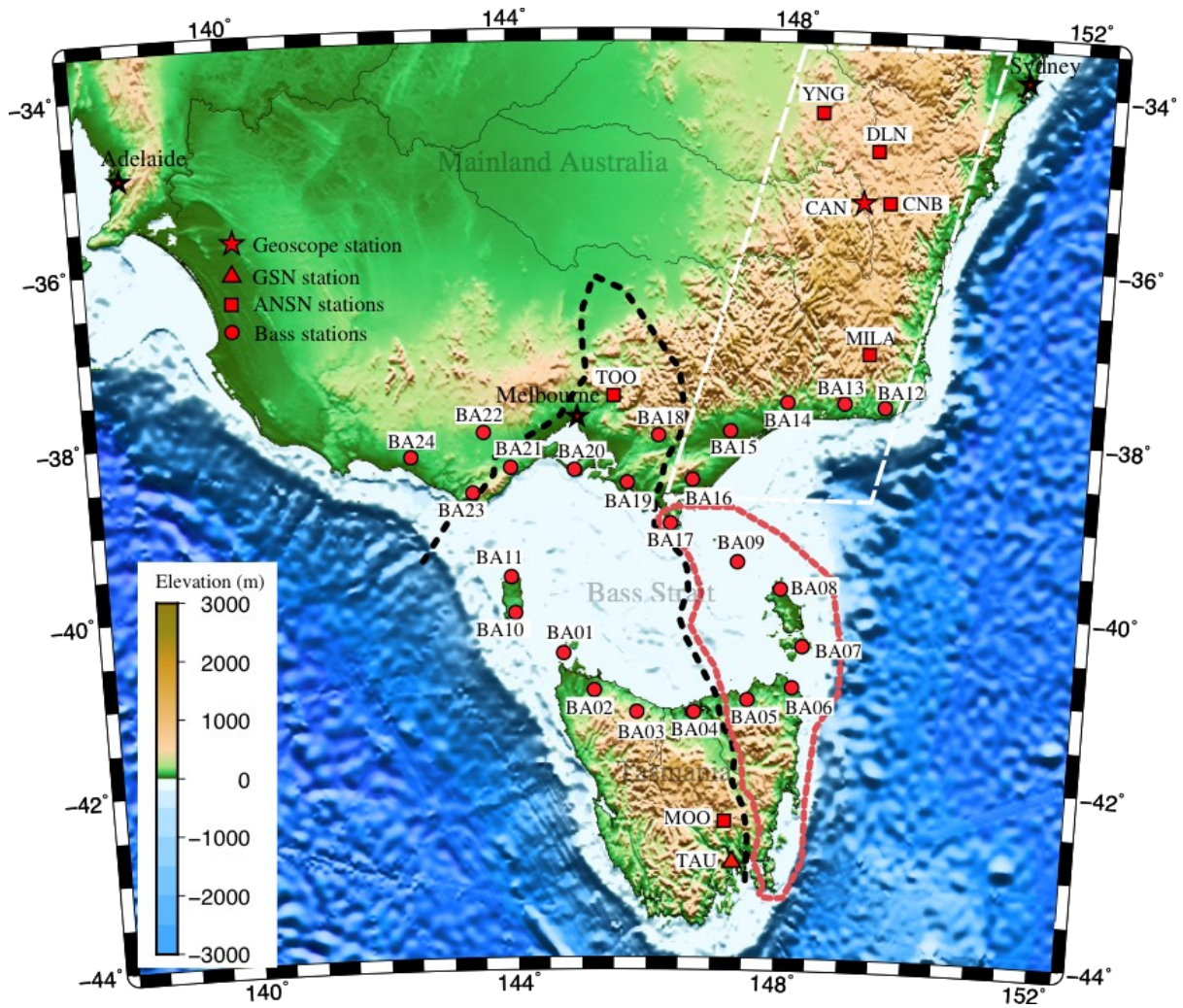
Figure 2: Location of seismic stations used in this study superimposed on a topographic/bathymetric map of southeast Australia (modified from Bello et al., 2019a). The boundary of VanDieland is delineated by a thick black dashed line. Thick red dashed line outlines the boundary of the East Tasmania Terrane and Furneaux Islands. Thick white dashed line highlights the eastern sector of the Lachlan Fold Belt. Topography/bathymetry is based on the ETOPO1 dataset (Amante and Eakins, 2009).
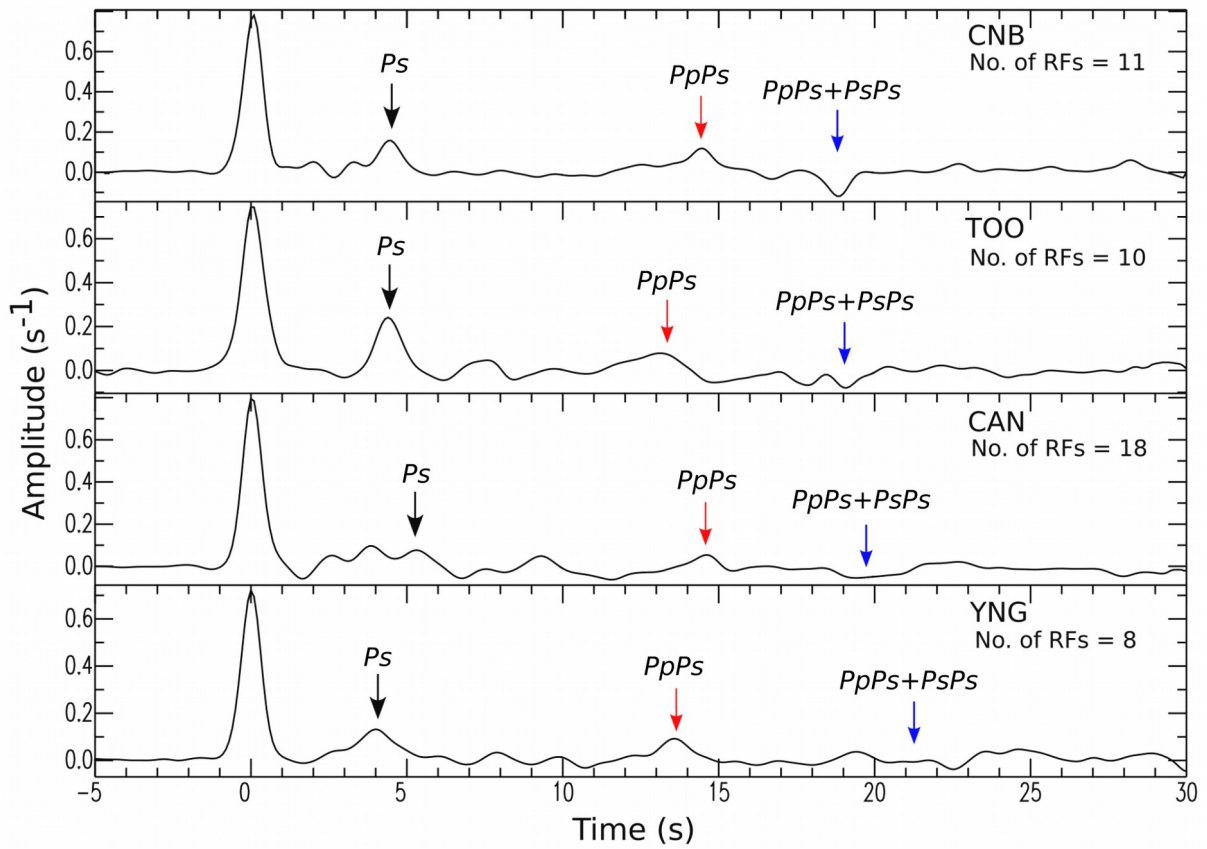
813
814
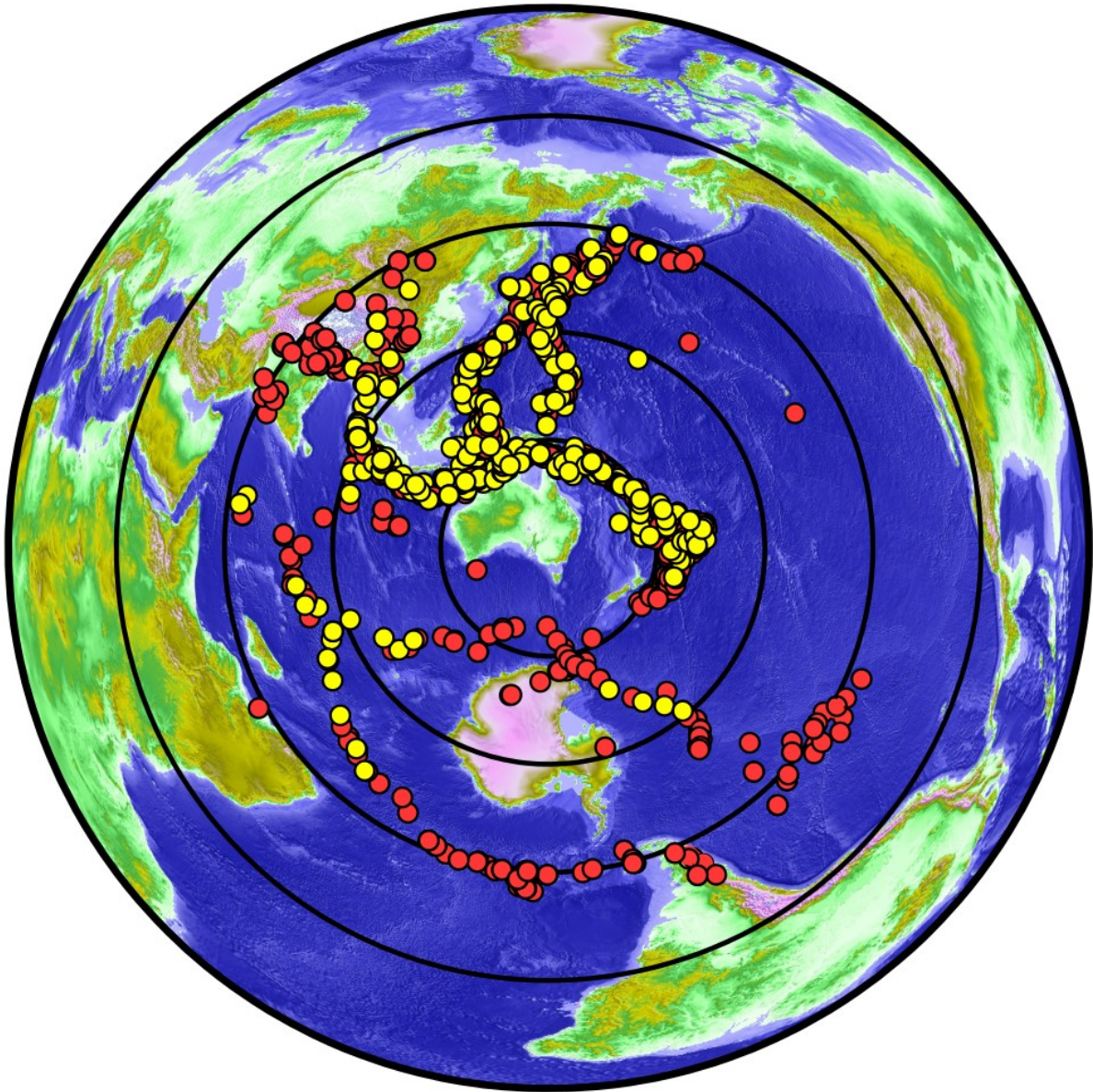
Figure 3: Distribution of distant earthquakes (teleseisms) used in this study. The locations of events that are ultimately used for RF analysis are denoted by yellow dots. Concentric circles are plotted at 30° intervals from the centre of Bass Strait. Topography/bathymetry colours are based on the Etopo1 dataset (Amante and Eakins, 2009).

819

Figure 4: Stacked receiver functions from Australian National Seismic Network (ANSN) stations TOO, YNG, MOO and GSN station TAU. Small arrows indicate arrival of the *Ps* (black), *PpPs* (red) and *PpPs + PsPs* (blue) phases from the Moho.

a)

Station: AU-MOO

Moho = 33.0 ± 1.2 km, Vp/Vs = 1.71 ± 0.04, Poisson's Ratio = 0.240 ± 0.019

Station: G-CAN

Moho = 39.1 ± 0.5 km, Vp/Vs = 1.73 ± 0.02, Poisson's Ratio = 0.250 ± 0.008

Station: AU-TOO

Moho = 37.5 ± 1.2 km, Vp/Vs = 1.68 ± 0.04, Poisson's Ratio = 0.226 ± 0.017

b)

Station: AU-MOO

33 km crust
Assumed Vp = 6.7 km/s
Vp/Vs for Symbols
Circle = 1.70
Diamond = 1.80
Square = 1.90

Station: G-CAN

39 km crust
Assumed Vp = 6.7 km/s
Vp/Vs for Symbols
Circle = 1.70
Diamond = 1.80
Square = 1.90

Station: AU-TOO

38 km crust
Assumed Vp = 6.7 km/s
Vp/Vs for Symbols
Circle = 1.70
Diamond = 1.80
Square = 1.90

828 **Figure 5: Results from the *H-κ* stacking analysis for RFs (Zhu and Kanamori, 2000) at stations MOO, CAN and**
829 **TOO. In each case (a) normalised amplitudes of the stack over all back-azimuths along the travel time curves**
830 **corresponding to the *Ps* and *PpPs* phases. (b) Corresponding stacked receiver function for each station.**

28

831

832
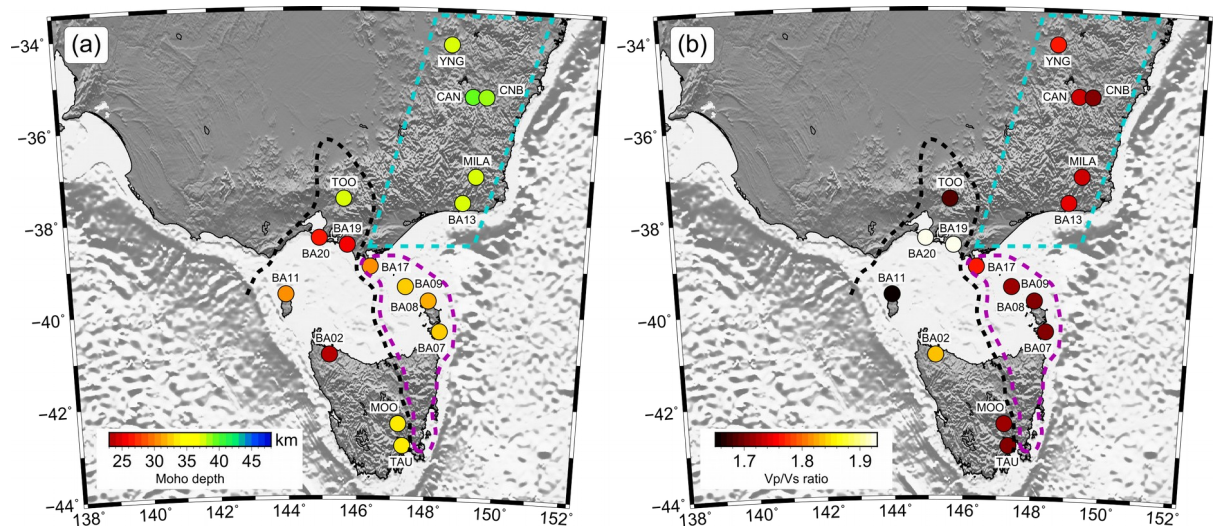
Figure 6: (a) Variations in crustal thickness and (b) *Vp/Vs* ratio taken from the linear (*H-κ*) stacking results (Table 2). Crustal thickness varies between ~23 and 39 km. *Vp/Vs* ratios vary from ~1.65 to 1.93. Thick black dashed line denotes the boundary of VanDieland. Thick magenta dashed line outlines the boundary of East Tasmania Terrane and eastern Bass Strait (ETT+EB). Thick cyan dashed line highlights the eastern part of the Lachlan Fold Belt. Illuminated topography/bathymetry is based on the Etopo1 dataset (Amante and Eakins, 2009).

29
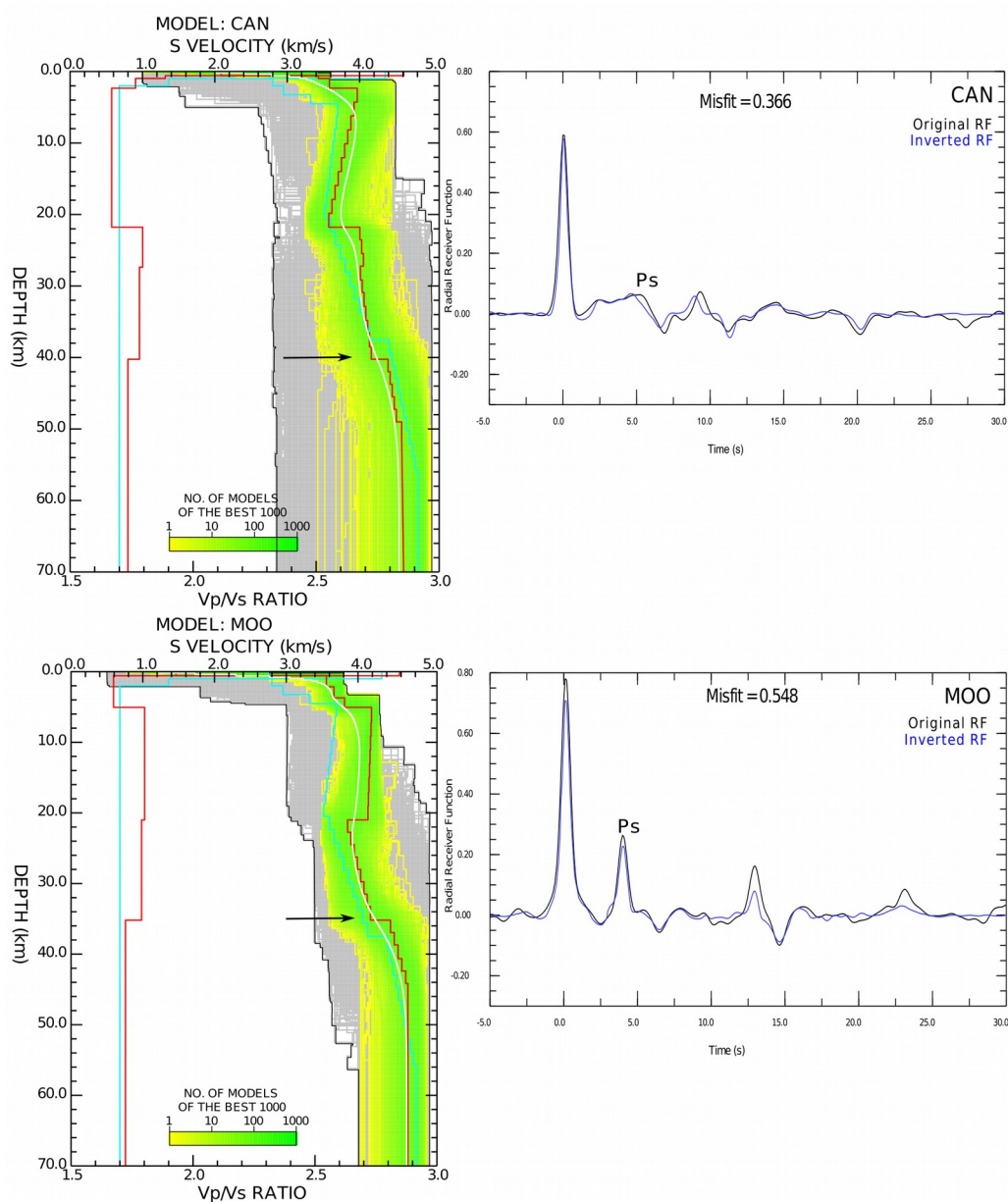
Figure 7: (Left) Seismic velocity models for CAN and MOO stations obtained from the neighbourhood algorithm (Sambridge 1999a). The grey area indicates all the models searched by the algorithm. The best 1000 models are indicated by the yellow to green colours; the best one (smallest misfit) corresponds to the red line, both for *S*-wave velocity (top horizontal axis) and *Vp/Vs* ratio (bottom horizontal axis) and the white line is the average velocity model. Small black arrows denote the estimated depth of the Moho. (Right) Waveform matches between the observed stacked receiver functions (black) and predictions (blue) based on the best models. "Misfit" refers to the chi-square estimate as defined by Equation 2.

849
850
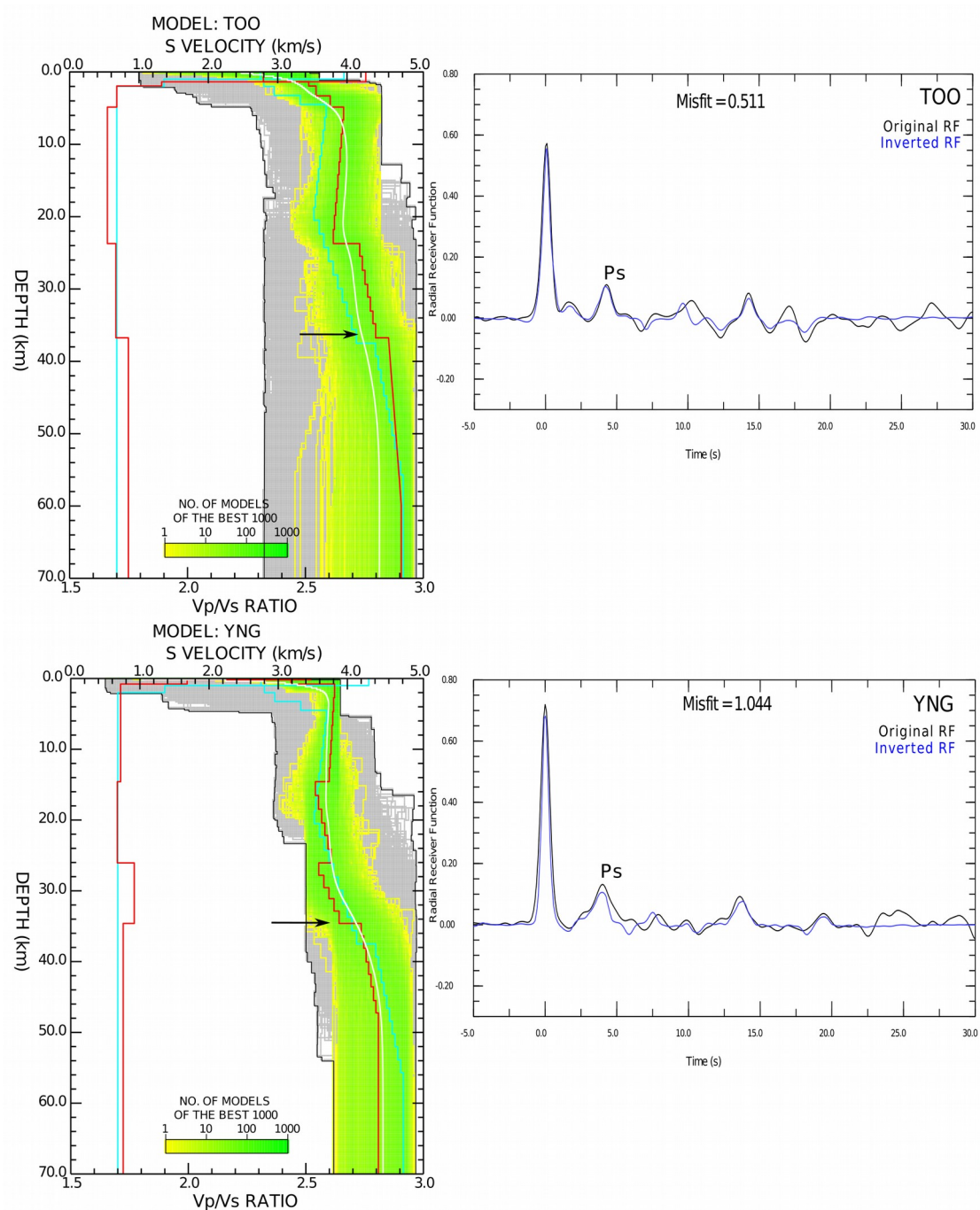
Figure 8: (Left) Seismic velocity models for stations TOO and YNG obtained from the neighbourhood algorithm. (Right) Comparison between the observed stacked and the predicted receiver functions from the NA inversion. See Figure 7 caption for more details.
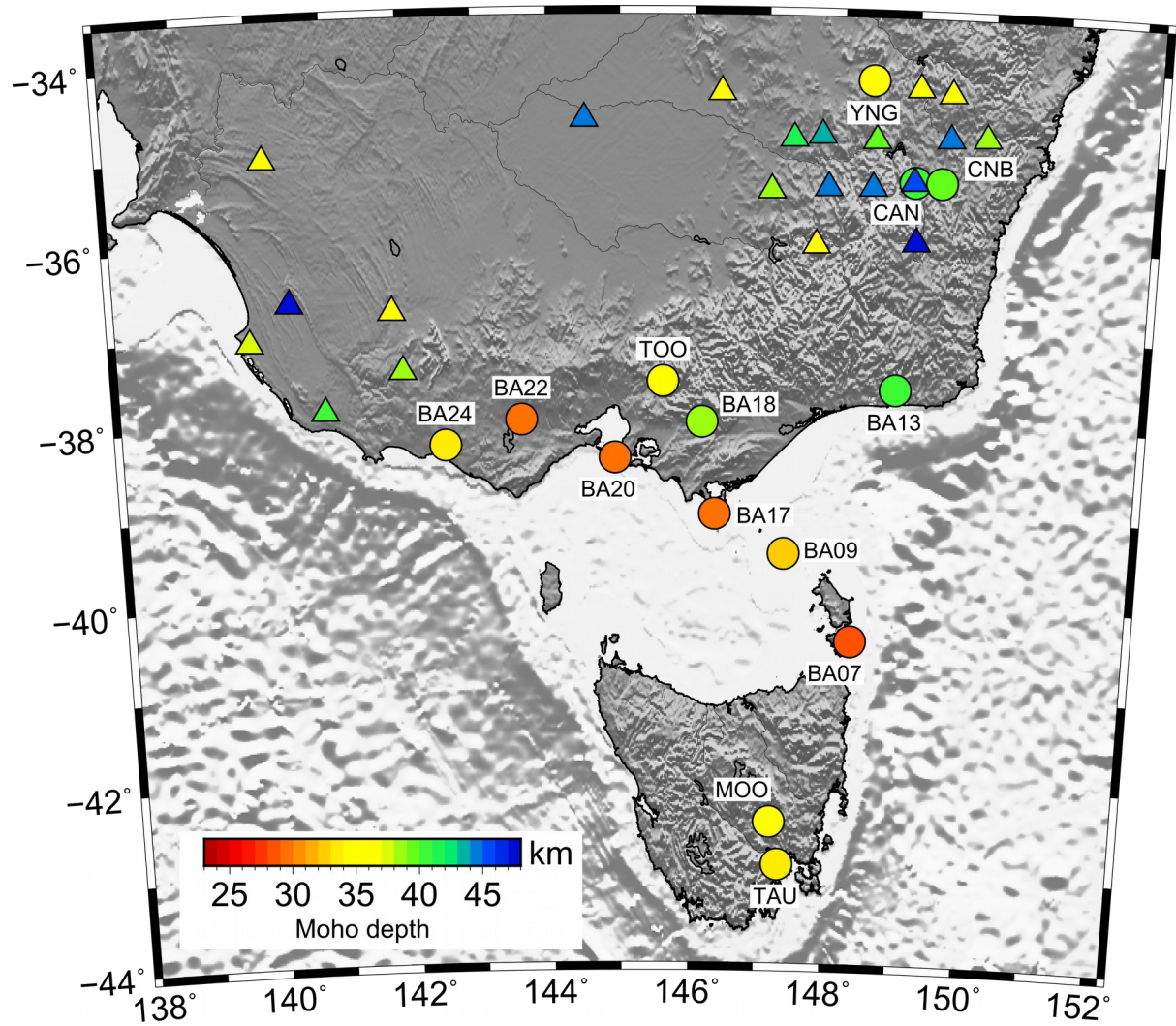
31
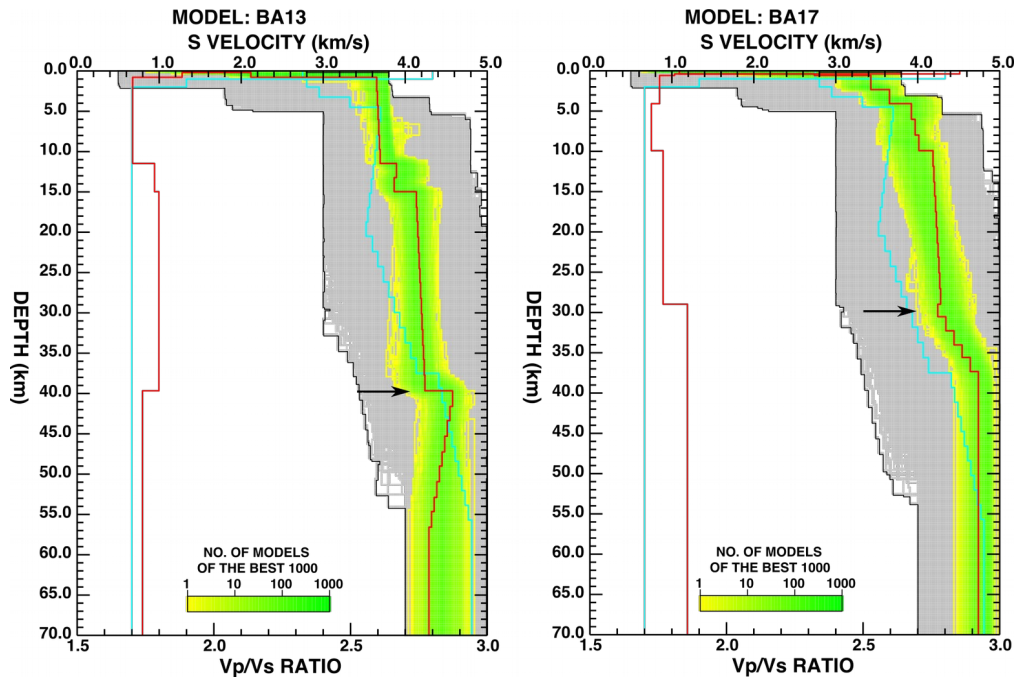
Figure 9: Seismic velocity models for temporary stations BA13 (left) and BA17 (right) obtained from the neighbourhood algorithm. See Supplementary Figures S6-S9 for all receiver function inversion results for the temporary BASS network, including waveform fits (Supplementary Figure S7 includes the waveform fit for stations BA13 and BA17).

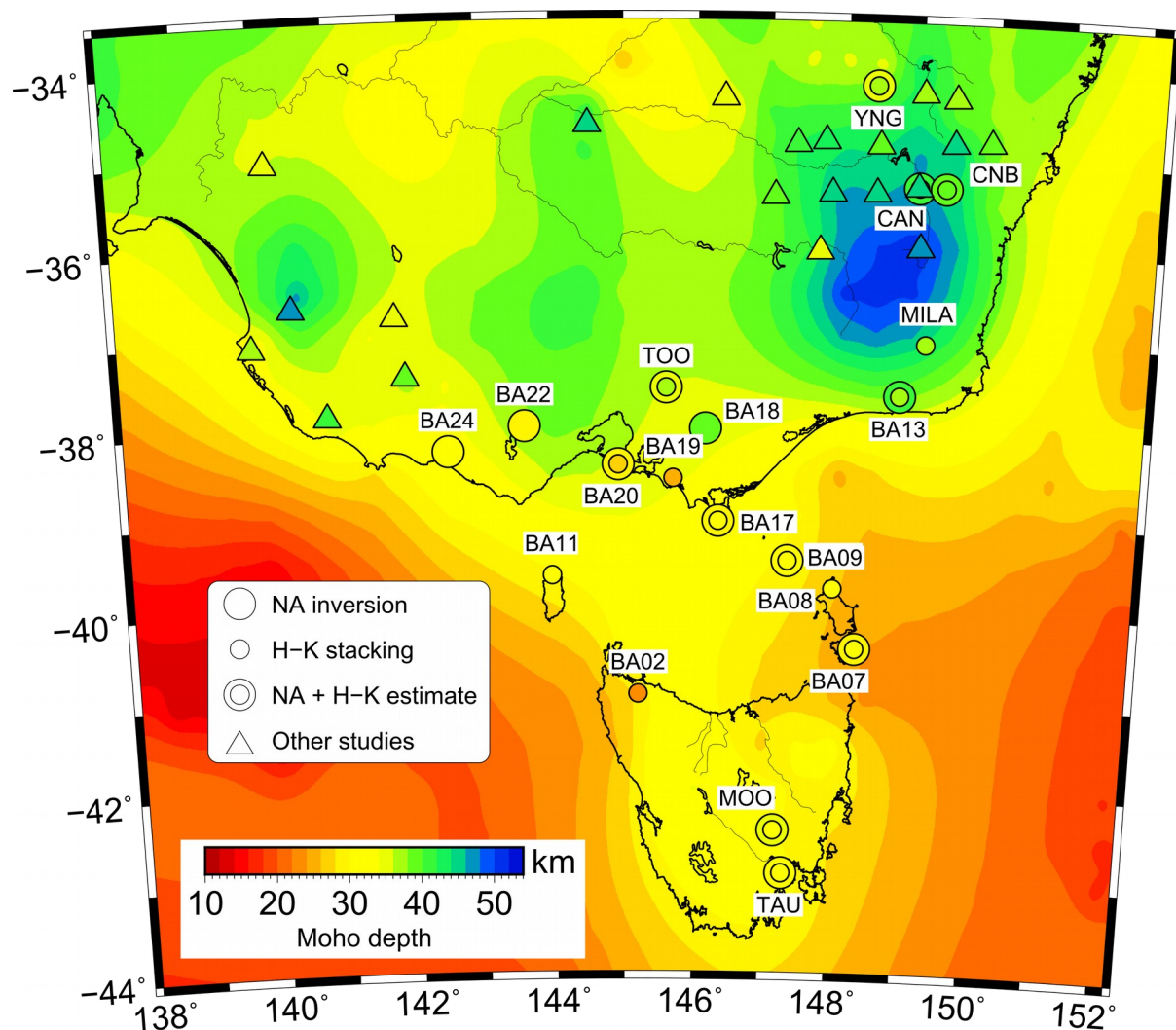**Figure 10:** Map showing crustal thickness variations based on the S-wave velocity inversion results of this study (circles) and previous studies (triangles) (Clitheroe et al., 2000, Fontaine et al., 2013a,b; Shibutani, 1996; Tkalcic et al, 2013). Topography/bathymetry is based on the Etopo1 dataset (Amante and Eakins, 2009).

Figure 11: Comparison between the AusMoho model (background colour map) and Moho depths determined through RF analaysis in this and previous studies. Small coloured circles denote the Moho depths determined from H-κ stacking, whereas large coloured circles correspond to receiver function estimates. When both H-κ and NA-derived depths are available at a single station, the smaller H-κ circle is superimposed on the larger NA circle, so that both depths can be observed on the one plot. Moho depths determined from previous RF studies are denoted by triangles.

880
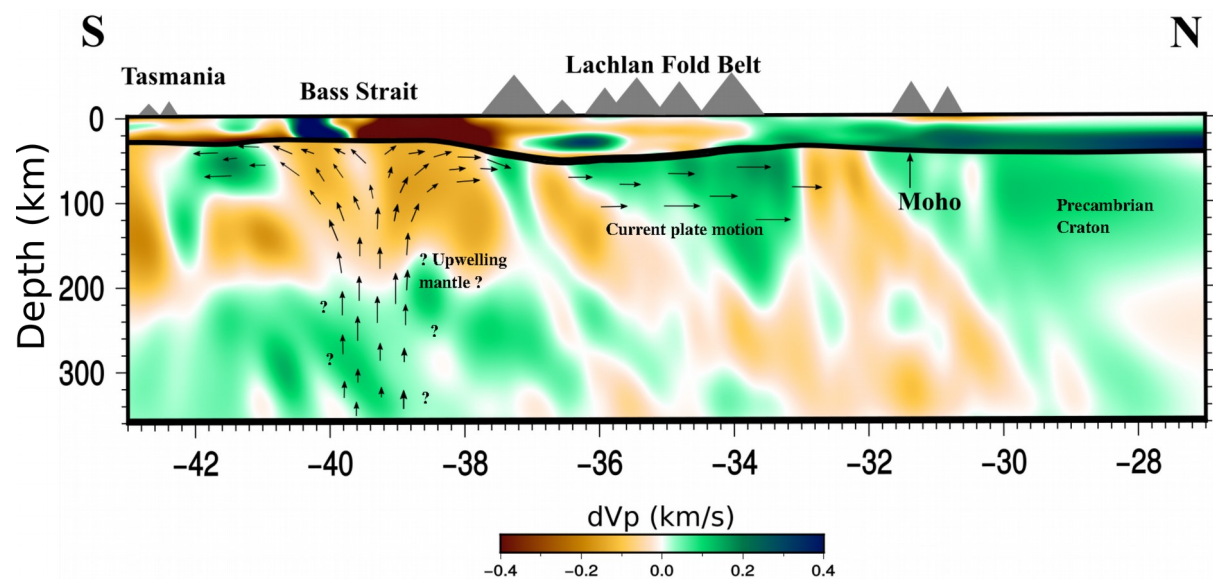
Figure 12: Composite result of teleseismic tomography (mantle velocity anomalies), ambient noise (crustal velocity anomalies), receiver functions (Moho) and shear wave splitting (inferred mantle flow relative to over-riding plate). Velocity slices are taken at 148ºE. Note that the the crustal model produced from ambient noise tomography is defined in terms of Vsv, but was converted to Vp in the study of Bello et al. (2019b) to permit its inclusion in the starting model for the inversion of teleseismic P-wave arrival time residuals. In this figure, the crustal Vp anomalies are shown.

889

890

891